Fibroblast state switching orchestrates dermal maturation and wound healing

Emanuel Rognoni[1,2], Angela Oliveira Pisco[1,2], Toru Hiratsuka[1], Kalle Sipilä[1], Julio Belmonte[3], Seyedeh Atefeh Mobasseri[1], Rui Dilão[4] and Fiona M. Watt[1]*

[1]Centre for Stem Cells and Regenerative Medicine, King's College London, 28thFloor, Tower Wing, Guy's Hospital Campus, Great Maze Pond, London SE1 9RT

[2]Equal contribution

[3]Developmental Biology Unit and Cell Biology and Biophysics Unit, European Molecular Biology Laboratory, Heidelberg, Germany

[4]Nonlinear Dynamics Group, Instituto Superior Técnico, Av. Rovisco Pais, 1049-001 Lisbon, Portugal

*Corresponding author: fiona.watt@kcl.ac.uk

Key words: dermis development, fibroblast states, mathematical modelling, tissue architecture, wound healing

Summary

Murine dermis contains functionally and spatially distinct fibroblast lineages that cease to proliferate in early postnatal life. Here we propose a mathematical model in which a negative feedback loop between extracellular matrix (ECM) deposition and fibroblast proliferation determines dermal architecture. Our model faithfully recapitulates dermal maturation, predicting a loss of spatial segregation of fibroblast lineages and dictating that fibroblast migration is only required for wound healing. To test this we performed *in vivo* live imaging of dermal fibroblasts, which revealed that homeostatic tissue architecture is achieved without active cell migration. In contrast, both fibroblast proliferation and migration are key determinants of tissue repair following wounding. The results show that tissue-scale coordination is driven by the interdependence of cell proliferation and ECM deposition, paving the way for identifying new therapeutic strategies to enhance skin regeneration.

Introduction

Mammalian skin comprises two mutually dependent layers, the epidermis and the dermis, which form through highly coordinated epithelial-mesenchymal interactions during development (Fuchs and Horsley, 2008; Watt, 2014). At embryonic day 12.5 (E12.5), mouse epidermis comprises one or two cell layers and the dermis appears homogeneous in composition. During development the dermis evolves from a multipotent pool of Pdgfrα^+ fibroblasts. These become lineage restricted at embryonic day 16.5 (E16.5), such that Lrig1 expressing fibroblasts give rise to the upper (papillary) dermis, while Sca1/Dlk1 positive fibroblasts give rise to the lower (reticular) dermis and hypodermis (Driskell et al., 2013).

The papillary dermis is distinguishable from the reticular dermis because of its higher cellular density and relative paucity of fibrillar collagen. Functionally the papillary lineage is required for hair follicle (HF) formation in skin reconstitution assays, whereas the lower lineage gives rise to the fibroblasts that mediate the initial phase of wound repair (Driskell et al., 2013; Rognoni et al., 2016). By postnatal day 2 (P2) the hypodermis has formed, comprising differentiated adipocytes and preadipocytes, while fibroblasts from the upper dermis differentiate into the HF arrector pili muscle. By P10 fibroblasts stop proliferating and dermal expansion results in separation of clonally related fibroblasts (Rognoni et al., 2016). In addition, resident immune cells, neuronal cells and endothelial cells are recruited, giving rise to the adult dermis.

It has been recently shown that epidermal cells coordinate a tissue-scale behaviour during wound repair, whereby the epithelium organizes directional migration and proliferation in overlapping regions oriented towards the wound (Aragona et al., 2017; Park et al., 2017). Upon wounding, dermal fibroblasts become activated, as evidenced by expression of α-smooth muscle actin (α-sma), start proliferating, migrate to the wound and deposit ECM, reconstituting the wound bed (Eming et al., 2014; Shaw and Martin, 2016). The upper and lower lineages enter the wound with different kinetics (Driskell et al., 2013; Rognoni et al., 2016) and adipocytes can be replenished from α-sma$^+$ fibroblasts (Plikus et al., 2017). However, how the growth and spatial organisation of dermal fibroblast subpopulations is regulated is currently unknown.

Here we elucidate how the tissue scale coordination of fibroblast behaviour is achieved during dermal development and homeostasis. Using a combination of cell biology techniques and mathematical modelling we were able to demonstrate that fibroblast behaviour switching between two distinct states – proliferating and depositing ECM - is necessary and sufficient to define dermal architecture. These cellular states are balanced by a negative feedback loop between ECM

deposition/remodelling and proliferation. Understanding the interdependence of cell behaviour and ECM is imperative for identifying new therapeutic strategies to enhance skin regeneration.

Results

Dermal maturation is driven by an inverse correlation between fibroblast proliferation and ECM deposition

By combining fibroblast density measurements with dermis volume calculations (Rognoni et al., 2016) we estimated the number of cell divisions during embryonic (E17.5 to P2) and postnatal (P2 to P50) growth (Fig 1A, Fig EV1A, Table EV1). Our data indicated that postnatally the dermis volume increased approximately 13 times with minimal proliferation, as our model only predicts 1.3 cell divisions. In contrary, during the embryonic stage the dermis volume increased proportionally to the change in cell number, indicating that perinatally tissue growth is driven by cell proliferation.

In line with this observation we found that most fibroblasts are proliferating ($Ki67^{+}$) at E10.5, but with age they progressively arrest in the G1 cell cycle phase, which we define as quiescence (Basak et al., 2017), without undergoing apoptosis (Rognoni et al., 2016) (Fig 1B upper panel, Fig 1C; Fig EV1B). The entry into quiescence coincided with a sharp increase in collagen deposition (quantified by Picrosirius red staining; Fig 1B lower panel). Quantitation of changes in proliferation and ECM deposition suggested an inverse correlation over time (Fig 1D), which led us to hypothesise that dermal growth consists of two phases. During the initial phase tissue expansion was due to proliferation, as the ratio of dermis volume to cell number is approximately 1:1. The second phase, corresponding to postnatal growth, was strongly associated with ECM deposition and remodelling, as between P2 and P50 the ratio of dermis volume to cell number is 4:1. These observations were supported by publicly available microarray data for neonatal and adult back skin fibroblasts, which showed that with age there was a reduction in genes associated with proliferation together with an enrichment for GO terms for ECM production and remodelling (Fig EV1C; (Collins et al., 2011; Rognoni et al., 2016)).

We further investigated the changes in the ECM by labelling with a collagen hybridizing peptide probe (CHP), which recognizes the triple helix structure of immature and remodelling collagen fibres (Fig EV2A, (Hwang et al., 2017)). Collagen fibre bundles were first detectable at E18.5 in the lower dermis, and in agreement with the Picrosirius red staining, further matured and expanded throughout the dermis with age. Moreover, ultrastructural analysis of P2 skin sections revealed that while there was no difference in collagen fibre diameter between upper and lower dermis, collagen fibre bundle formation was evident in the lower dermis whereas only small and dispersed collagen fibres were present in the upper dermis (Fig EV2B,C). At P2 the fibroblasts closest to the basement membrane were more proliferative than those in the lower dermis (Fig 1E,F; Fig EV2D). This emphasized that the relationship between ECM deposition and fibroblast quiescence held within

different regions of the dermis at any given time point. We observed the same correlation when we examined human foetal and adult tissue sections (Fig 1G-I). We therefore concluded that dermal fibroblasts exhibit differential growth behaviour at distinct developmental time points and dermal locations, either dominated by cell proliferation or ECM production.

Modelling a switch between two fibroblast states

To create a mathematical model deconstructing the inverse correlation between proliferation and ECM production we assumed that fibroblasts switch between two states, proliferating fibroblasts (PF, with proliferating rate κ_1) and quiescent fibroblasts (QF), with transition rates κ_2 and κ_{-2} (Fig 2A, File EV1). Following the experimental observations we conjectured that the existence of ECM would negatively regulate PF (κ_4), pushing the equilibrium towards a state where PF were minimal and both QF and ECM deposition/remodelling were maximal. The derived ordinary differential equation (ODE) model is shown in Fig 2B. To fit the experimental data, we defined our multi-objective optimization problem adapted to the particularity of having two data sets to fit (PF and ECM, Fig 1D) and followed a Monte Carlo technique to find the solutions (Fig 2C; File EV1; (Dilão et al., 2009; Dilão and Muraro, 2010; Dilão and Sainhas, 2011; Muraro and Dilão, 2013)). For the parameters obtained, our model had one stable state for which all variables (PF, QF and ECM) were non-negative: that corresponded to the adult dermis. We concluded that a simple model whereby ECM represses fibroblast proliferation via a negative feedback loop was the key element setting dermal architecture.

A 3D tissue model recapitulates dermal maturation

In order to test the mechanism of fibroblast behaviour and spatial organisation during dermal maturation, we developed a 3D model in Compucell3D (Belmonte et al., 2016; Hirashima et al., 2017; Swat et al., 2012). We conceptualized the whole animal as a cylindrical object but focused on modelling the dermis between neighbouring hair follicles, to avoid considering changes in the skin associated with the hair growth cycle (Donati et al., 2014). We initialized our body segment model as a simple cylindrical segment, where epithelial tissue (green) surrounded the proliferative fibroblasts enclosing a lumen representative of the inside of the animal body (white) (Fig EV3A). To explore the fundamental dermal architecture, we solely focused on dermal fibroblast behaviour and excluded other cell types, such as immune, neuronal or endothelial cells.

Since fibroblasts close to the basement membrane were more proliferative (Fig 1E,F; Fig EV2D) and the switch in fibroblast behaviour also correlated with a decrease in basal keratinocyte

proliferation (Fig EV3B), we proposed that the differential spatial proliferation of fibroblasts during development was influenced by an epidermal gradient (Fig EV3C, (Collins et al., 2011; Lichtenberger et al., 2016)). Epidermal signal strength was assumed to decline with age, accounting for the decline in proliferation. Therefore, in this model, the epidermal gradient directly impacted on the fibroblast division capability. Moreover, in our mechanism the presence of ECM directly affected fibroblasts in the proliferative state. To account for that behaviour, we linked the transition from the proliferative state to quiescence with the amount of ECM surrounding the cell committing the decision.

While both proliferating and quiescent fibroblast populations could produce ECM, in line with the model in Fig 2A, quiescent cells deposited and remodelled ECM more efficiently. Additionally, fibroblasts in direct contact with the lumen were able to differentiate into adipocytes in a spatially defined manner (Driskell et al., 2014). We included an adipocyte layer to represent the process of fibroblast differentiation into adipocytes, based on experimental data demonstrating the timing of appearance of the dermal white adipose tissue (DWAT; (Rognoni et al., 2016)), but further modelling of the DWAT maturation during development was not considered.

The fundamental tissue-scale behaviour of the dermis was fully recapitulated in our spatial model (Fig 3A-C, Movie EV1). We started with a pool of proliferative fibroblasts that respond to the presence of the epidermal gradient (MCS 0, ~E10.5). When the proliferative cells became surrounded by ECM, the cells stopped dividing and deposited ECM more efficiently. The cells in the lower dermis differentiated into adipocytes (MCS>300) in a spatially controlled manner, that is, only cells in direct contact with the body wall would be able to do so. At the first step of dermal maturation we went through a phase of homogeneous tissue (MCS<100), where we had minimal amount of ECM and all cells were proliferative. Next, proliferating cells switched to a quiescent state, increasing ECM deposition, and the proliferative rim converged to the region around the epidermis (MCS ~200, ~E17.5). After MCS>300 (~P0), cells close to the lumen differentiated into adipocytes, forming the hypodermis layer. After MCS>450 (~P5) all proliferation ceased and the dermis started expanding due to the accumulation of ECM. As a reference, the model progression was optimized such that MCS=300 coincided with the *in vivo* proliferation data measured at P0 (for full details please refer to the Methods section).

Fibroblast organisation occurs without active cell migration during dermal maturation

We drew two predictions from the computational model: dermal organization is achieved without fibroblast migration and there is no spatial segregation of fibroblasts in adult dermis.

In P2 dermis there is clear spatial segregation of the papillary and reticular dermis (Driskell et al., 2013). However, without explicitly modelling active fibroblast migration, *in silico* lineage tracing indicated that fibroblasts lying closest to the epidermis dispersed throughout the dermis over time and eventually started contributing to the adipocyte layer (Fig 3D,E). Lower dermal fibroblasts also dispersed but rarely moved into the upper dermis (Fig 3F). The computational simulations were consistent with *in vivo* lineage tracing data. Fibroblasts from the upper dermis (labelled with Blimp1Cre or Lrig1CreER) became dispersed through out the dermis, whereas lower dermal fibroblasts (labelled with DlkCreER) were predominantly confined to the lower dermis and DWAT (Fig EV3D,E; (Driskell et al., 2013; Lichtenberger et al., 2016; Rognoni et al., 2016)). To examine whether or not there is fibroblast movement within adult dermis we performed *in vivo* live imaging of the back skin of adult mice. We recorded the same field of cells continuously for up to 200 min and detected only minimal cell movement (Fig 3G, Movie EV2), consistent with the prediction of the computational model.

Together, our experiments and simulations demonstrated that no active cell migration was required to generate the architecture of the mature dermis. Instead, our simulations suggested that dermal fibroblasts became gradually displaced over time as a consequence of the switching between the two states, driving tissue expansion.

The proliferation-ECM negative feedback loop restores tissue homeostasis following wound healing

Our computational model indicates a unidirectional shift from the proliferating state to the state of ECM production during dermal maturation. However, it is well established that upon wounding dermal fibroblasts become activated and re-start proliferating. How these changes are coordinated on the tissue scale, such that the regular architecture is re-established, is unknown.

To test the fibroblast state reversibility we created 2 mm diameter circular full thickness wounds on adult back skin and analysed them at different locations and time points (Fig 4A,B). Upon wounding, fibroblasts close to the wound became rapidly activated and the expression of α–sma peaked at post wounding day 7 (PW7) (Fig 4C,D; Fig EV4A). We observed high fibroblast proliferation in the upper and lower wound bed during the early phases of wound repair, suggesting that fibroblasts in different locations exit their quiescent state with identical probabilities (Fig 4E,F, Fig EV4B). By PW7 fibroblasts reached their maximal cell density in the wound bed centre, exceeding the density outside the wound (Fig 4G). This coincided with the first appearance of collagen fibres, with randomized orientations in the upper and lower wound bed (Fig 4H, Fig

EV4C). During the advanced wound healing phase (>PW10) most fibroblasts stopped proliferating (Fig 4F,I). At PW15 fibroblasts in the wound bed centre were still activated and had a higher density than in the surrounding tissue, while collagen fibres were less mature (Fig 4C-H, Fig EV4C). In the late wound healing phase (>PW21) keratinocyte proliferation at the wound site remained high, while fibroblast density was restored to normal (Fig 4I).

When comparing fibroblast proliferation with ECM accumulation in the wound bed, we observed that the inverse correlation was recapitulated inside the injured area (Fig 5A). Outside the wound there were only minor changes in collagen or fibroblast density (Fig 5B), indicating that only fibroblasts close to the wound site were actively involved in the repair process. To determine whether the switch from quiescence back to proliferation determined the observed kinetics of wound healing, we revisited the mathematical model in Fig 2 (File EV1). As the experimental data points towards a de-novo accumulation of cells inside the wound bed, the model was expanded with the additional assumption that proliferating (PF) and quiescence fibroblasts (QF) at the boundary of the wound could move. Under these conditions, the spatial structure of the dermis was described by the partial differential equation model in Fig 5C, where ***D***, the diffusion coefficient, represented cell motility. The qualitative behaviour of our mathematical model corroborated the experimental data. Accordingly, there was an increase in proliferation during the initial repair phase (4 days after wounding; Fig 5D). Our mathematical model thus showed that the introduction of a diffusion coefficient was necessary and sufficient to allow the proliferation/ECM negative feedback loop to describe the fibroblast behaviour observed during skin regeneration (Fig 5E, Movie EV3).

Active cell migration is essential for efficient wound repair

We next revisited our spatial model to investigate the kinetics of fibroblast proliferation, migration and ECM deposition during wound healing. We simulated a 2 mm wound on adult mice (MCS 1200, ~P50; Fig 6A) by removing a tissue slice and associated gradients, and filling the space with a blood clot (red cells in the simulation) and infiltrating immune cells (purple cells in the simulation). These cells added a local wound healing gradient that decayed over time post-wounding, mimicking the pro-proliferative effect of the blood clot and the infiltrating immune cells on the surrounding fibroblasts *in vivo* (Fig EV5A) (Eming et al., 2014). We modelled fibroblast response to tissue wounding disregarding cell position in the tissue. Accordingly, fibroblasts in the vicinity of the wound became activated (cells in pink in the simulation) in response to the local and temporally restricted wound healing gradient and re-entered the high proliferation state. We introduced cell migration in the form of movement towards the wound healing gradient for the cells that were in the

vicinity of the wound, enabling activated fibroblasts to invade the wound bed. The epidermis also proliferated in response to the wound healing gradient, which promoted the migration of proliferating keratinocytes to close the wound.

With this expanded model our simulations were able to recapitulate the steps of the wound healing process and dissect the distinct fibroblast state/behaviour changes (Fig 6A, Movie EV4). Upon wounding fibroblasts became activated and accumulated at the wound edge. While epidermal cells closed the wound and isolated the blood clot, activated fibroblasts invaded the space occupied by the immune cells and displaced them, before depositing and remodelling the ECM. At the later stage, during wound resolution, the cells around the wound area entered quiescence, restoring tissue physiology.

Since our models predicted that active cell migration is necessary for dermal repair and our spatial simulation corroborated the finding, we decided to investigate the fibroblast migration kinetics *in vivo*. As before, we created 2 mm diameter circular wounds and repeatedly imaged them at the indicated time-points (Fig 6B). Maximum projections of Z-stack images of the whole wound area revealed a sharp increase in fibroblast density at the wound borders 4 days post wounding (Fig 6C). No fibroblast migration was observed at PW2 (Fig EV5B, Movie EV5), whereas at PW4 we observed fibroblasts rapidly migrating into the wound bed (Fig 6D, Fig EV6A, Movie EV6). Fibroblast migration stopped by PW7 (Fig EV6B), correlating with the appearance of collagen fibres in the wound bed (Fig EV4C). The lack of active migration at PW15, when fibroblast density in the wound bed was still high, suggested that fibroblasts were dispersed while ECM was actively deposited and remodelled (Fig EV6C, Movie EV7). This was shown by the higher CHP signal in the wound bed even after PW21 (Fig EV4C).

To investigate whether fibroblasts from different locations expanded with different probabilities during wound repair, we performed lineage tracing experiments by crossing Confetti reporter mice either with Blimp1Cre mice, labelling fibroblasts in the upper dermis, or with Dlk1CreER mice, labelling fibroblasts in the lower dermis (Fig 6E; (Driskell et al., 2013)). When analysing the clonal distribution 10 days post wounding, we observed that clones of the upper and lower dermis were able to expand and redistribute in the entire wound bed, independently of their initial location (Fig 6F-H). Thus, the tissue scale model, the *in vivo* imaging and lineage tracing revealed that fibroblasts of the upper and lower dermis accumulate at the wound edges and migrate into the wound bed, before expanding and dispersing through the entire wound bed.

Discussion

In this study we demonstrated that mouse dermal expansion is driven by two sequential growth phases – pre- and post-natal – each dependent on cellular state switching. Using a combination of *in vivo* and *in silico* techniques we showed that dermal architecture is established by a negative feedback loop between the deposition/remodelling of ECM and fibroblast proliferation. The temporally regulated switch from proliferation to quiescence is sufficient to achieve the tissue scale coordination of fibroblast behaviour observed during dermal development and homeostasis. Together, our experimental data and validated tissue simulations support a model whereby fibroblast migration is the critical discriminator between dermal development and wound healing.

During both dermal maturation and repair, tissue architecture is established via a switch between fibroblast proliferation and ECM deposition. Proliferating fibroblasts progressively enter a quiescence state for efficient ECM production and remodelling. The presence of ECM promotes the cellular switch from the proliferative state towards the quiescent state and leads to cell separation via ECM-mediated displacement (Fig 7 – Development). As a general principle, coordinated tissue growth and homeostasis require many cell types, including stem cells and fibroblasts, to stop dividing and acquire a quiescent state (Cheung and Rando, 2013). This state is defined as a controlled and reversible cell cycle arrest, which can last for years. In cell culture, human diploid fibroblasts can enter quiescence in response to signals such as contact inhibition, loss of adhesion or starvation, which are not present *in vivo* (Coller et al., 2006). Interestingly these different quiescence stimuli induce distinct gene expression signatures, indicating that quiescence is the manifestation of a collection of states rather than a common cell cycle arrest state (Coller et al., 2006; Sang and Coller, 2009a). Furthermore, cellular quiescence is an actively maintained state, not a solo consequence of cell cycle arrest, as neither CDK inhibition nor overexpression of CDKI induce a quiescence-specific gene expression program (Coller et al., 2006; Sang and Coller, 2009b).

Many functional changes occur during induction of cellular quiescence, including changes in metabolism, autophagy, gene expression and chromatin structure (Lemons et al., 2010). Surprisingly, besides actively reinforcing the non-dividing cell cycle state and repressing the transition into senescence or terminal differentiation, quiescent fibroblasts remain highly metabolically active. They increase expression of ECM proteins such as Col I and III, which is partly due to changes in expression of miRNAs such as miR-29, and in line with these findings, the quiescence gene signature is enriched in GO terms for ECM proteins (Suh et al., 2012). While the processes that drive fibroblast quiescence *in vitro* have been relatively well described, the signalling

networks that stimulate and maintain quiescence of dermal fibroblasts *in vivo* are still unknown. Moreover, it is not known whether distinct fibroblast subpopulations exhibit different quiescence regulation mechanisms. Nevertheless, our microarray data suggests a role for chromatin, given that sorted fibroblast at different ages show distinct signatures for GO terms such as chromatin assembly, DNA packaging and protein-DNA complexes organisation. This is compatible with the observed fast and reversible fate switching from quiescence to proliferation during wound healing.

Before wounding, the adult mouse has a steady state distribution of fibroblasts in a quiescent state and associated ECM deposition (Fig 7 – homeostasis). Upon wounding there is a local change in the concentration of cells and ECM and the system is no longer at steady state. In response to this, at very early stages of wound repair fibroblasts actively migrate towards the wound bed and switch back to a proliferative state, a behaviour that is not restricted to a specific dermal layer (Fig 7 – tissue injury). Our integrative approach revealed that, in contrast to the observed behaviour during dermal development, not only proliferation but also fibroblast migration were essential in the early wound healing phase. At later stages fibroblasts in the wound bed recapitulate the dermal maturation process by exiting the cell cycle, allowing for efficient ECM deposition and remodelling. To restore normal cell density, the wound bed fibroblasts are gradually dispersed by the newly synthesized and remodelled ECM, without the requirement of active cell migration. This sequence of changes in fibroblast behaviour during wound healing suggests that migration, proliferation and ECM metabolism are coordinated processes leading to a reshuffling of fibroblast organisation.

Our proposed mathematical model demonstrates that dermal homeostasis can be achieved by a repressive mechanism in which the deposition of ECM promotes fibroblasts to stop proliferating. The resulting negative interaction is justified by the observation that the increase in collagen concentration is accompanied by the decrease in PF cells. On the other hand, the depletion of ECM during wounding, leading to regeneration, shows that when the repressor is absent fibroblasts restart to proliferate. To achieve regeneration at the wound position, the simplest mechanism is to allow the motility of fibroblasts. This motility is induced by the imbalance of fibroblast concentrations near the wound, which is a diffusive process. Thus, the mechanism whereby ECM deposition blocks proliferation holds true for tissue perturbation and defines the key element for re-establishing tissue architecture upon wounding.

In skin, pathologies linked to quiescence can range from fibrosis, where there is excessive fibroblast activity following injury, or chronic wounds, where quiescent fibroblasts fail to re-enter the cell cycle and coordinate the wound healing response. Furthermore, tumour and tumour stroma cells seem to adopt cellular quiescence mechanisms to ensure long-term survival and escape

chemotherapy-mediated killing (van Deursen, 2014). By developing a computational model we were able to recapitulate the fundamental processes leading to the tissue-scale behaviour during development, homeostasis and wound healing. Our model enabled us to deconstruct at single cell level the events that happen during tissue regeneration, making it a promising tool to investigate response to injury, disease and treatment strategies.

Acknowledgements

F.M.W. gratefully acknowledges financial support from the Medical Research Council and Wellcome Trust. E.R. is the recipient of an EMBO long-term fellowship (ALTF594-2014); T.H. is the recipient of a Marie Skłodowska Curie Fellowship; and K.S. is the recipient of a Finnish Cultural Foundation Fellowship. We are grateful to Yang Li (University of Utah) for providing Collagen Hybridizing Peptide and Gema Vizcay-Barrena of the KCL Centre for Ultrastructural Imaging for technical support. We thank the Nikon Imaging Centre and BSU staff at KCL for expert assistance. We also acknowledge the use of Core Facilities provided by the generous financial support from the Department of Health via the National Institute for Health Research (NIHR) comprehensive Biomedical Research Centre award to Guy's & St Thomas' NHS Foundation Trust in partnership with King's College London and King's College Hospital NHS Foundation Trust.

Author contributions

ER and AOP conceptualized the study, designed the experiments, delineated the mathematical modelling and analysed the results. ER performed *in vivo* experiments. AOP performed mathematical modelling and bioinformatics analysis. TH performed the *in vivo* live imaging. KS performed the Picrosirius red stainings and quantifications. JB assisted with the Compucell3D modelling. SAM performed TEM imaging and quantification. RD assisted the model design and implementation of the 1D simulations. ER and AOP wrote the manuscript and produced the Figs. FMW oversaw the study and co-wrote the manuscript.

Conflict of interest

The authors declare no conflict of interest

Materials and Methods

Transgenic mice and lineage tracing

All experimental procedures were carried out under the terms of a UK Home Office project license after local ethical review at King's College London. All mice were maintained on a C57BL6/CBA background and male and female mice were used in experiments. All mice were outbred on a C57BL6/CBA background and male and female mice were used in experiments that included Blimp1-Cre (Robertson et al., 2007), Dlk1CreERt2 (Driskell et al., 2013), Lrig1CreER (Page et al., 2013), PDGFRαH2BeGFP (Hamilton et al., 2003), ROSAfl-stopfl-tdTomato (Jackson Laboratories, 007905), CAGCATeGFP (Kawamoto et al., 2000), Dermo1Cre (Jackson Laboratories, 008712), R26Fucci2a (Mort et al., 2014) and Confetti mice (Snippert et al., 2010). For *in vivo* cell cycle analysis, R26Fucci2a was crossed with Dermo1Cre and back skin was analysed at the indicated time-points.

For lineage tracing transgenic reporter mice were crossed with the indicated Cre or CreER lines. CreER was induced by injection with 10µl Tamoxifen (50 µg/g body weight) (Sigma-Aldrich) intraperitoneally in new-born mice (P0), when DLK1 and Lrig1 are highly expressed in dermal fibroblasts (Driskell et al., 2013; Rognoni et al., 2016). After embryonic development Blimp1 is not expressed in dermal fibroblasts, except for dermal papilla cells, enabling us to lineage tracing upper dermis (papillary) fibroblasts during development and wound healing (Donati et al., 2017; Driskell et al., 2013; Telerman et al., 2017). Tamoxifen for injection was dissolved in corn oil (5 mg/ml) by intermittent sonication at 37°C for 30 min. Tissue was collected at the indicated time points, briefly fixed with paraformaldehyde/PBS (10 min at room temperature), embedded into Optimal Cutting Temperature compound (OCT) and horizontal wholemounts or thin 12 µm thick sections were prepared. Horizontal wholemount sections were mounted in glycerol and immediately imaged with a Nikon A1 Confocal microscope using 10X or 20X objectives. Only YFP, CFP and RFP labelled cells in Confetti mice were analysed, because the frequency of nuclear GFP labelled cells was very low. All labelled cells of one colour within a 260±50 µm radius (Driskell et al., 2013; Rognoni et al., 2016) were scored as being clonally related.

Wound healing

Wound healing assays were performed as previously described (Rognoni et al., 2016). Briefly, analgesic EMLA cream (AstraZeneca) was applied topically to the back skin of adult mice 10 min before mice were anaesthetised using Isoflurane (Cp-pharma). A 2 mm punch biopsy (Stiefel) was

used to make a full-thickness wound in the central back skin. Back skin was harvested at the time points indicated after wounding.

Histology and microscopy

Human foetal skin was obtained with appropriate ethical approval from the UK Human Developmental Biology Resource (www.hdbr.org). Adult surgical waste skin was obtained from the King's Health Partners Cancer Biobank (HTA Licence No: 12121, REC No: 12-EE-0493). Mouse and human tissue samples were embedded in OCT prior to sectioning. For confocal imaging, cryosections of 12 µm thickness were fixed with 4% paraformaldehyde/PBS (10 min at room temperature), permeabilised with 0.1% TritonX100/PBS (10 min at room temperature), blocked with 5% BSA/PBS (1 hour at room temperature) and stained with the following primary antibodies to: Vimentin (Cell signaling, #5741), CD26 (R&D Systems, AF954), Sca1 (BD Pharmingen, clone E13-161.7), GFP (abcam, ab13970 and A-11122, ThermoFisher), Ki67 (abcam, ab16667), α−sma (Abcam, ab5694) and CD49f (BioLegend, clone GoH3). Samples were labelled overnight at 4°C, washed in PBS, and labelled with secondary antibodies and 4,6-Diamidino-2-phenylindole (DAPI) (1µg/ml diluted 1:50000; ThermoFisher) for 1 hour at room temperature. Samples were mounted with ProLong® Gold Antifade Mountant media (ThermoFisher). 60 µm horizontal whole-mount sections were immunostained as described previously (Rognoni et al., 2016). Confocal microscopy was performed with a Nikon A1 Confocal microscope using 10X or 20X objectives. Image processing was performed with Nikon ND2 Viewer Software, Image J (Fiji), Photoshop CS6 (Adobe) and Icy (version 1.6.0.0) software.

Collagen analysis

For collagen quantification 12 µm cryosections from the back skin were stained with Picrosirius red using a standard method (Lattouf et al., 2014). Briefly, the sections were fixed (7 min, 4 % PFA), washed twice with water, and stained for 1 hour in Picrosirius red solution (0.1% Sirius red F3B (Sigma) in saturated aqueous solution of picric acid). After staining, sections were washed twice with acidified water (0.5 % acetic acid), dehydrated, cleared with xylene, and mounted with DPX mounting medium (Sigma). The images were taken with a Zeiss Axiophot microscope and AxioCam HRc camera under plane polarized light that shows the collagen fibers as green, orange, and yellow against a black background. The intensity of light was adjusted to give a linear response for quantification. The quantification of total collagen fibres was performed using Fiji Image software. The collagen pixels were selected with the Colour Threshold tool (Hue 0-100, Saturation

0-255, and Brightness 230-255) and the binary images were created based on the selection. Collagen density was determined by dividing the area of collagen pixels by total tissue area. Total tissue area was manually cropped from the basement membrane to fat cells excluding hair follicles. For Collagen Hybridizing Peptide (CHP) staining (Hwang et al., 2017; Li et al., 2012) 12 µm cryosections of back skin were fixed with 4% paraformaldehyde/PBS (10 min at room temperature), permeabilised with 0.1% TritonX100/PBS (10 min at room temperature), blocked with 5% BSA/PBS (1 hour at room temperature) and stained with the indicated primary antibodies and 5 µM B-CHP (BIO300, 3Helix) overnight at 4°C. According to the Manufacturer's instructions the B-CHP probe was heated for 5 min at 80°C before adding it to the primary antibody mix, which was immediately applied to the tissue sections. Sections were washed three times with PBS and incubated with appropriate secondary antibody and Streptavidin-AlexaFluor647 (S32357, ThermoFisher) for 1 hour at room temperature. After washing the sections with PBS and incubating them with DAPI (1 µg/ml diluted 1:50000) for 10 min at room temperature, the samples were mounted with ProLong® Gold Antifade Mountant media (ThermoFisher). Confocal microscopy was performed with a Nikon A1 Confocal microscope using 10X or 20X objectives.

Transmission Electron Microscopy (TEM)

Transmission electron microscopy of mouse dorsal skin was performed by the Centre for Ultrastructural imaging at King's College London following fixation in 4% paraformaldehyde/PBS for 1 hour. TEM (JOEL JEM) was used to obtain images from upper and lower dermis. Using ImageJ (FIJI), 250X250 nm random areas were selected and collagen fibre diameter and collagen fibre density were measured.

Flow cytometry and cell cycle analysis

Dermal fibroblasts were isolated at indicated time points, as previously described (Collins et al., 2011; Jensen et al., 2010). Briefly, back skin was incubated for 1 hour in dispase-trypsin solution at 37°C, after which the epidermis was separated from the dermis and discarded. The dermis of neonatal mice was minced and incubated in 0.25% collagenase in FAD medium at 37°C for 1 hour. Adult dermis was minced and incubated in FAD medium containing 1.25 mg/ml collagenase type I (Invitrogen), 0.5 mg/ml collagenase type II (Worthington), 0.5 mg/ml collagenase type IV (Sigma), 0.1 mg/ml hyaluronidase IVS (Sigma) and 50 U/ml DNase I at 37°C for 1 hour. Enzyme activity was neutralised by the addition of serum-containing medium.

The dermal cell suspension was passed through a 70 µm cell strainer, washed twice with PBS and labelled with the following antibodies according to standard procedures: CD26 PercPcy5.5 (eBioscience, 45-0261), Ly-6A/E PE (eBioscience, Clone D7), CD45 APC (eBioscience, Clone), CD31 APC (eBioscience, Clone D7), CD234 APC (eBioscience, Clone D7) and Dlk1 PE (MBL International, D187-5). DAPI was used to exclude dead cells. Labelled cells were sorted on a BD FACSAria Fusion. For cell cycle analysis isolated cells were fixed with 70% EtOH for 1 hour at 4°C, washed with PBS and treated with 250 µl RNAse A (Sigma) (100 µg/ml in PBS) for 15 min at room temperature. Prior to FACS analysis with a BD FACSCanto II cells were incubated with 25 µl Propidium Iodide (Sigma) (500µg/ml stock solution) for 10 min at room temperature and cells were gated for GFP^+ expression. Data analysis was performed using FlowJo software version 7.6.5 (Tree Star, Ashland, OR).

Microarray analysis

We reanalysed the previously published microarrays GEO GSE32966 (Neonatal (P2) and P50 back skin PDGFRaH2BeGFP fibroblast; (Collins et al., 2011)).

***In vivo* live imaging**

In vivo live imaging was performed as described in (Hiratsuka et al., 2015). In brief, two-photon excitation microscopy was performed with an A1RMP upright microscope, equipped with a 25X/1.10 water-immersion objective lens (CF175 Apo LWD 25XW Nikon) and a Ti:Sapphire laser (0.95 W at 900 nm) (Coherent Chameleon II laser). The laser power used for observation was 2–10%. Scan speed was 4 µs/pixel. The excitation wavelength was 770 nm for Second harmonic generation. Z stack images were acquired with a view field of 0.257 mm^2 in 5 µm steps and for whole wound maximum projections images were stitched together.

For adult mouse back skin imaging the fur was clipped and hair follicles were removed with depilation cream 1 hour before wounding or 24 hours before imaging unwounded skin. Imaging was started at the time points indicated. Throughout imaging mice were anesthetized by inhalation of vaporized 1.5% isoflurane (Cp-pharma) and placed in the prone position in a heated chamber maintained at 37°C. The back skin was stabilized between a cover glass and a thermal conductive soft silicon sheet as previously described (Hiratsuka et al., 2015). The wound healing process was imaged at the indicated days after wounding. Time-lapse images were acquired every 30 min. A total of 2 mice per time point were examined and the duration of timelapse imaging was 5 ± 2hrs per mouse. Time-lapse imaging was aborted if the body temperature, breathing condition, or

hydration of a mouse deteriorated. Optimisation of image acquisition was performed to avoid fluorescence bleaching and tissue damage and to obtain the best spatiotemporal resolution. Acquired images were analysed with MetaMorph (Universal Imaging, West Chester, PA) and Fiji imaging software (Image J, NIH). The fibroblasts of the PdgfrαH2BeGFP transgenic mice can be readily detected because of nuclear GFP expression (Collins et al., 2011) and the fibrillar collagen of the dermis is autofluorescent, enabling ready visualisation.

Mathematical modelling

Calculation of cell division rate The calculation of cell division rate has been described previously (Rognoni et al., 2016). Briefly, height, length and dermis diameter were measured (n=3 mice per time point and gender) and the dermis volume was estimated by representing the mouse trunk as a cylinder. Cell densities were obtained from Fig 1A,B and the cell numbers at E17.5 (N_E), P2 (N_N) and P50 (N_A) were estimated by multiplying cell density and dermis volume. The predicted cell division rate is calculated by the $\log_2$ of the $N_{older}/N_{younger}$ ratio.

1D ODE model The negative feedback loop between proliferating fibroblasts and ECM was modelled using an ODE system in Mathematica. For a full description please refer to File EV1.

Tissue model: Glazier Graner Hogeweg/ Cellular Potts simulations The Glazier Graner Hogeweg/Cellular Potts Model (GGH/CPM) represents a single cell as an extended domain of sites (pixels) on a regular lattice that share a common index σ. For detailed information about GGH/CPM see (Belmonte et al., 2016; Swat et al., 2012). Our CC3D model computer code is available upon ask. In brief, a cellular Potts model was implemented using the CompuCell3D platform (Swat et al., 2012). Cells in this model are represented as connected domains on a grid with the cell-free area represented as a special domain. Chemoattractant concentrations are represented on the same grid. Cell dynamics result from a series of attempts to expand the domains at randomly selected grid sites. Whether an expansion attempt is accepted or not depends on a set of rules, which thus determine cell dynamics. Simulations represent a 3D section of mouse skin. Fibroblasts are initialized as 10 cells disposed radially in contact with the epidermis (wall boundary conditions) and surrounding the body cavity (lumen). Built-in routines were used for the implementation of chemotaxis and secretion. Lumen and epidermal integrity, cell divisions, cell differentiation, cell fate conversion and wound healing were implemented as custom steppables.

Quantification and statistical analysis

Data analysis was performed with GraphPad Prism 7 software. Unless stated otherwise, data are means ± standard deviation (s.d.). The spot detector plugin of Icy software (version 1.6.0.0) was used for unbiased identification and quantification of cells labelled with RFP, CFP or CFP (Confetti lineage tracing) and cell nuclei labelled with DAPI, Ki67, R26Fucci2a or PDGFRαH2BEGFP. Cell densities and lineage traced cells were quantified from at least eight 12 µm or 60 µm horizontal skin whole mounts or wound bed sections per mouse.

Figure legends

Fig 1. Dermal architecture is defined by an inverse correlation between fibroblast proliferation and ECM deposition.

(A) Quantification of fibroblast density (number of PDGFRαH2BEGFP$^+$ cells, left; n=3 biological replicates per time point) and dermis volume (right) with age (n=7 E12.5; n=8 P0, P6; n=9 E16.5, E17.5, P4; n=10 P10, P50; n=11 E10.5; n=12 E18.5, P2, P21; n=20 P12 biological replicates). (B) Changes in fibroblast proliferation and collagen deposition during dermal development in mice. Immunofluorescence staining for Ki67 (red) of PDGFRαH2BEGFP (green) back skin at indicated developmental time points (upper panel). Polarised light images of Picrosirius red stained back skin sections shown in binary images at indicated time points (lower panel). (C) Percentage of PDGFRαH2BEGFP$^+$ cells in G1 cell cycle phase with age (n=1 E12.5; n=2 P2, P10; n=3 E16.5, E17, P0; n=4 E10.5; n=5 E17.5, E18.5, P50; n=7 P4 biological replicates) fitted using an exponential model. (D) Quantification of fibroblast proliferation (left; n= 4 E16.5, P10; n= 3 E10.5, E18.5, P2, P21, P44, P50; n= 2 E17.5, P0 biological replicates) and collagen density (right; n= 4 E16.5, P2, P6, P10, P14, P16, P21, P50; n= 3 E10.5, E18.5, P2, P21, P44, P50 biological replicates) with age. (E) Immunofluorescence image of R26Fucci2axDermo1Cre back skin at P2 where mVenus-hGem (green) expressing cells are in S/G2/M phase and mCherry-hCdt1 (red) positive cells are arrested in G1 phase. (F) Percentage of labelled cells in S/G2/M cell cycle phase in the upper and lower dermis at P0 (n=3 biological replicates) and P2 (n=4 biological replicates). (G-I) Changes in dermal cell proliferation and collagen deposition in human skin. (G) Immunofluorescence staining for Vimentin (red) and Ki67 (green) of back skin at indicated time points (upper panel). Polarised light image of Picrosirius red stained back skin section shown as binary image at indicated time points (lower panel). (H) Quantification of proliferating cells in the upper and lower dermis (n=3 biological replicates per time point). (I) Quantification of dermal cell

proliferation ($Ki67^+$) (left) and collagen density (right) with age (n= 3 biological replicates per time point). Note that cells in upper human dermis were more proliferative than cells in the lower dermis at all developmental time points analysed and that fibroblasts entered a quiescent, non-proliferative state before collagen was efficiently deposited. Data shown are means ±s.d. Nuclei were labelled with DAPI (blue in B,E,G).Scale bars, 100μm.

Fig 2. A negative feedback-loop between ECM and proliferation determines fibroblast state switching.

(A) Schematic representation of the assumed relationships between proliferating fibroblasts (PF), quiescent fibroblasts (QF) and extracellular matrix (ECM) during dermal maturation. PF self-replicate with rate κ_1. PF and QF can switch among them with rates κ_2 and κ_{-2} respectively. QF deposit ECM at rate κ_3. ECM promotes the switch from PF to QF at rate κ_4. (B) System of ordinary differential equations (ODE) describing the process of dermal maturation. Because the system is dynamic, all entities can decay over time (κ_6 is the degradation rate of QF, κ_7 is the degradation rate of ECM, κ_5 is the degradation rates of PF and is incorporated into β as $\beta = \kappa_1 GF - \kappa_2 - \kappa_5$). (C) Resulting simulation of the system of equations in (B) and experimental data in Fig 1D, with the optimized parameters from File EV1.

Fig 3: Development of a 3D tissue model and *in vivo* live imaging during dermal maturation.

(A) (*x,y*) cross-section of the computational model simulation of the dermal maturation process at the indicated Monte-Carlo Steps (MCS). Colour code indicates epidermis (green), proliferating fibroblasts (blue), quiescent fibroblasts (yellow), ECM (grey) and adipocytes (brown). See accompanying Movie EV1. (B) Abundance of the cell populations during the course of the simulation. (C) Quantification of fibroblast proliferation and ECM density in the simulation. (D-F) *In silico* lineage tracing of fibroblasts. (D) Labelling of fibroblasts close to the epidermis at indicated MCS. (E) Labelling of fibroblasts in the middle of the dermis at indicated MCS. (F) Labelling of fibroblasts close to the inside of the body at indicated MCS. (G) Live imaging of adult PDGFRαH2BEGFP mouse back skin. Representative time-lapse images of adult PDGFRαH2BEGFP (green) dermis with collagen (second harmonic generation in purple) at indicated imaging time points. Scale bar, 100 μm. See accompanying Movie EV2.

Fig 4: Fibroblast proliferation and ECM changes during wound healing.

(A,B) Experimental design of wound healing time course analysis. (A) Wound healing time course. Skin was collected at the indicated time points. (B) Quantification strategy is schematically illustrated. Red boxes: upper dermis; black boxes lower dermis; solid lines inside and dashed lines outside the wound site. (C,D) Fibroblast activation during wound repair. Immunofluorescence staining for α−sma (red) of PDGFRαH2BEGFP wound sites at indicated post wounding (PW) times (C) and quantification of α−sma fluorescence intensity in pixel per area inside the upper and lower wound bed (n= 4 PW0, PW2, PW7, PW21; n= 3 PW10, PW14; n= 2 PW4 biological replicates) (D). (E-H) Changes in fibroblast density, proliferation and collagen deposition during wound repair. (E) Immunostaining for Ki67 (red) of PDGFRαH2BEGFP (green) back skin sections at indicated wound healing time points. (F) Quantification of fibroblast proliferation in the upper and lower dermis inside the wound bed over time (n= 4 PW0, PW2, PW21; n= 3 PW4, PW10; n= 2 PW7, PW14 biological replicates). (G) Quantification of fibroblast density during wound repair inside and outside the wound bed (n= 4 PW0, PW2, PW21; n= 3 PW4, PW10; n= 2 PW7, PW14 biological replicates). (H) Polarised light image of Picrosirius red stained back skin section shown as binary image at indicated time points after wounding. (I) Quantification of proliferating (Ki67 positive) keratinocytes and fibroblasts during wound repair over time (n= 4 PW0, PW2, PW21; n= 3 PW4, PW10; n= 2 PW7, PW14 biological replicates).

Fig 5: The negative feedback-loop between ECM and proliferation is necessary and sufficient to restore tissue architecture.

(A,B) Quantification of fibroblast proliferation (left; n= 4 PW0, PW2, PW21; n= 3 PW4, PW10; n= 2 PW7, PW14 biological replicates) and collagen density (right; n= 4 PW0, PW2; n= 3 PW4, PW7, PW10, PW14; n= 2 PW21 biological replicates) inside (A) and outside (B) the wound bed over time. (C) System of partial differential equations describing the process of dermal wound healing. The system in Fig 2B was expanded to incorporate the diffusion coefficient D with the associated spatial term. (D) Temporal evolution of proliferating fibroblasts (PF) and dermal ECM density over time. The model is able to describe the qualitative behaviour observed in Fig 5A. (E) Simulation of dermal wound closure showing the distribution of PF (blue), QF (yellow) and ECM (green) at the time of wounding and at two subsequent time points. From left to right, we performed a wound by imposing that both proliferating cells and ECM are zero in a specific region and simulate the wound healing process during time with the model equations in Fig 5C. Note that the system re-establishes the original densities, corroborating the experimental data that only the region directly associated with the wound was affected (File EV1). Please refer to associated Movie EV3.

Fig 6: 3D model and *in vivo* live imaging of dermal wound repair.

(A) *(x,y)* cross-section of the computational simulation of wound healing in adult dermis. (B-D) Live imaging of adult PDGFRαH2BEGFP back skin during wound healing. Please refer to associated Movie EV4. (B) Experimental design of *in vivo* imaging of wound healing. (C) Representative wound bed Z-stack stitched maximum projections of the entire wound bed (upper panel) showing fibroblasts (green) and collagen (second harmonic generation in purple) at indicated time points after wounding and before live imaging. Dotted line indicates wound edge and boxed area indicates the position of the magnified area bellow. (D) Representative time-lapse images of adult wound bed at PW4, where Z-directional movement is visualized by pseudo colouring the fibroblast nuclei (red, movement towards the basement membrane; blue, movement away from the basement membrane). Dotted line indicates wound edge. Please refer to associated Movie EV6 which shows fibroblasts actively migrating into the wound bed. (E-H) *In vivo* lineage tracing of upper (Blimp1Cre) and lower (Dlk1CreER) dermal fibroblasts during wound healing. (E) Experimental strategy for *in vivo* lineage tracing. (F) Immunofluorescence image of Blimp1Cre x Confetti (upper panels) and Dlk1CreER x Confetti (lower panel) back skin inside and outside the wound bed at 10 days post wounding. Colours show YFP (green), RFP (red) and CFP (blue) with bright field image overlaid. (G) Clone size quantification of Blimp1Cre labelled fibroblasts inside and outside the wound bed at 10 days post wounding (n= 400 clones of 4 biological replicates). (H) Clone size quantification of Blimp1Cre labelled fibroblasts inside and outside the wound bed at 10 days post wounding (n=300 clones of 2 biological replicates). Scale bars, 500μm (C); 100μm (D,F).

Fig 7: Schematic of how fibroblast state switching determines tissue architecture.

During development the tissue scale behaviour of dermal fibroblasts is achieved and maintained by a feedback loop between ECM deposition and fibroblast switching from proliferating to quiescent. Upon wounding, quiescent cells re-enter the cell cycle and tissue regeneration occurs via the sequential coordination of proliferation, active migration and cell displacement in the wound bed.

Expanded View Fig legends:

Fig EV1 (related to Fig 1): Correlating changes in epidermis and dermis with mouse development

(A) Modelling dermal fibroblast cell divisions during development (adapted from Rognoni et al., 2016). Predicted number of dermal fibroblast divisions during the transition from embryonic (E17.5)

to neonatal (P2) and neonatal (P2) to adult (P50) mouse. Height, length and dermis diameter were measured (n=3 mice per time point and gender) and the dermis volume was estimated by representing the mouse trunk as a cylinder. Cell densities were obtained from Fig 1A and cell number at E17.5 (N_E), P2 (N_N) and P50 (N_A) was estimated by multiplying cell density and dermis volume. The predicted cell division rate is calculated by the $\log_2$ of the $N_{older}/N_{younger}$ ratio. Calculated values are shown in Table EV1. (B) Representative cell cycle flow cytometry profiles for indicated time points. Note the sharp decrease in S-phase with age and the arrest in G1. (C) Comparative analysis of the transcriptomics of neonatal and adult mouse fibroblasts (GSE32966). The volcano plot (left panel) illustrates the sharp differences in the fibroblast gene expression of different ages. Colour code indicates entities not statistically significantly changed (grey), statistically significant but not enriched (green) or significantly changed with fold change >2 and p-value smaller than 0.05. Red corresponds to enriched in neonatal and blue to enriched in adult. Gene ontology (GO) analysis (right panel) of neonatal and adult fibroblasts. GO terms are highlighted in neonates (red) and adults (blue).

Fig EV2 (related to Fig 1): Distinct collagen structure in the upper and lower neonatal dermis

(A) Immunofluorescence staining of back skin sections at indicated developmental time points for Itga6 (green) and Collagen (red) using the CHP-Biotin probe. Nuclei were labelled with DAPI (blue). Note the appearance of collagen fibers after E18.5. (B) TEM image of upper (papillary layer, left) and lower (reticular layer, right) dermis at P2. Boxed area is magnified below. (C) Quantification of collagen fibre diameter (upper panel; n=42 fibres) and density (lower panel) in upper and lower dermis at P2 (n=10 1µm^2 regions). (D) Quantification of proliferating fibroblasts (Ki67$^+$ cells) in the upper and lower dermis at indicated time points (n=3 E18.5; n=2 P0 biological replicates). Scale bars: 100µm (A), 2µm (B).

Fig EV3 (related to Fig 3): Skin proliferation kinetics and fibroblast lineage tracing during dermal maturation *in vivo* and *in silico*

(A) 3D visualization of the simulated mouse body segment. (B) Quantification of proliferating (Ki67 positive) keratinocytes and fibroblasts in skin over time (n= 4 E16.5, P10; n= 3 E10.5, E18.5, P2, P21, P44, P50; n= 2 E17.5, P0 biological replicates). Note that the decrease in proliferation of keratinocytes and fibroblasts follows similar kinetics over time. (C) Representative simulation images of the epidermal gradients at indicated MCS. Note that the signal concentrates in the immediate surroundings of the epidermal cells and decays over time. (D,E) *In vivo* lineage tracing

of upper (Blimp1$^+$ or Lrig1$^+$ cells) and lower dermis (Dlk1$^+$ cells) fibroblasts. (D) Immunofluorescence image of tdtomato or CAG-EGFP labelled fibroblasts (red) with the indicated Cre lines. (E) Quantification of the percentage of labelled fibroblasts in the lower dermis of adult mice (>P50) (n= 2 biological replicates). Note the increased abundance of Blimp1- and Lrig1-CreER labelled dermal fibroblasts in the lower dermal layer with age.

Fig EV4 (related to Fig 4): Changes in fibroblast activation and proliferation outside the wound and CHP staining in the wound bed

(A) Quantification of α−sma fluorescence intensity in pixels per unit area in the upper and lower dermis outside the wound bed (n= 4 PW0, PW2, PW7, PW21; n= 3 PW10, PW14; n= 2 PW4 biological replicates). (B) Quantification of fibroblast proliferation in the upper and lower dermis outside the wound bed over time (n= 4 PW0, PW2, PW21; n= 3 PW4, PW10; n= 2 PW7, PW14 biological replicates). (C) Immunofluorescence staining of adult PDGFRαH2BEGFP (green) wounds at indicated time points for collagen (red) using the CHP-biotin probe. Note that collagen fibres are appearing at PW7 in the upper and lower wound bed. Nuclei were labelled with DAPI (blue). Data shown are means ± s.d. Scale bar, 100μm.

Fig EV5 (related to Fig 6): Computational wound healing gradients and *in vivo* imaging of the wound bed at PW2

(A) Gradients used in the computational model. Top panel represents the wound healing gradient during the course of the simulation. Bottom panel represents the epidermal gradient in the vicinity of the wound during the course of the simulation. (B) Representative time-lapse images of adult PDGFRαH2BEGFP (green) dermis and collagenous extracellular matrix (second harmonic generation in purple) 2 days after wounding. Dotted line indicates wound edge. Note that fibroblasts are not actively migrating at 2 days post wounding. Please refer to associated Movie EV5. Scale bar, 100μm.

Fig EV6 (related to Fig 6): *in vivo* imaging of the wound bed at later time points

(A-C) Representative time-lapse images of adult PDGFRαH2BEGFP (green) dermis with collagenous extracellular matrix (second harmonic generation in purple) 4 days (A), 7 days (B) and 15 days (C) after wounding. Dotted line indicates wound edge. Note that fibroblasts are actively migrating at 4 but not at 7 or 15 days post wounding. Please refer to associated Movies S6 and S7. Scale bars, 100μm.

Expanded View Files

File EV1 (related to Figs 2 and 5): Deduction of the 1D ODE model of dermal maturation and regeneration post wound healing.

Expanded View Tables

Table EV1 (related to Fig 1 and Fig EV1): Calculations of total body volume, dermal volume and number of cell divisions.

Expanded View Movies

Movie EV1 (related to Fig 3): Computational simulation of dermal maturation. Sequential key MCS of the simulation are shown in Fig 3A.

Movie EV2 (related to Fig 3): *In vivo* live cell imaging of dermal fibroblasts (green) and collagen (purple) in adult PDGFRαH2BEGFP back skin of adult mice. Sequential time-lapse images are shown in Fig 3G.

Movie EV3 (related to Fig 5): Computational simulation of the wound repair in the 1D Ode model. Sequential key steps are shown in Fig 5E.

Movie EV4 (related to Fig 6): Computational simulation of wound repair of adult skin (MCS:1200). Sequential key MCS of the simulation are shown in Fig 6A.

Movie EV5 (related to Fig EV5): *In vivo* live cell imaging of dermal fibroblasts (green) and collagen (purple) in adult PDGFRαH2BEGFP back skin wound at 2 days post wounding. Sequential time-lapse images are shown in Fig EV5B.

Movie EV6 (related to Fig 6): *In vivo* live cell imaging of dermal fibroblasts at in adult PDGFRαH2BEGFP back skin wound area at 4 days post wounding. Sequential time-lapse images are shown in Fig 6D and Fig EV6A (without pseudo colouring). Note that z-directional movement is visualized by pseudo colouring the fibroblast nuclei (red, movement towards the basement membrane; blue, movement away from the basement membrane). Dotted line indicates wound edge.

Movie EV7 (related to Fig EV6): *In vivo* live cell imaging of dermal fibroblasts (green) and collagen (purple) in adult PDGFRαH2BEGFP back skin wound area at 15 days post wounding. Sequential time-lapse images are shown in Fig EV6C.

References

Aragona, M., Dekoninck, S., Rulands, S., Lenglez, S., Mascré, G., Simons, B.D., and Blanpain, C. (2017). Defining stem cell dynamics and migration during wound healing in mouse skin epidermis. Nat Commun *8*, 14684.

Basak, O., Beumer, J., Wiebrands, K., Seno, H., van Oudenaarden, A., and Clevers, H. (2017). Induced Quiescence of Lgr5+ Stem Cells in Intestinal Organoids Enables Differentiation of Hormone-Producing Enteroendocrine Cells. Cell Stem Cell *20*, 177–190.e4.

Belmonte, J.M., Clendenon, S.G., Oliveira, G.M., Swat, M.H., Greene, E.V., Jeyaraman, S., Glazier, J.A., and Bacallao, R.L. (2016). Virtual-tissue computer simulations define the roles of cell adhesion and proliferation in the onset of kidney cystic disease. Mol. Biol. Cell *27*, 3673–3685.

Cheung, T.H., and Rando, T.A. (2013). Molecular regulation of stem cell quiescence. Nat. Rev. Mol. Cell Biol. *14*, 329–340.

Coller, H.A., Sang, L., and Roberts, J.M. (2006). A new description of cellular quiescence. PLoS Biol. *4*, e83.

Collins, C.A., Kretzschmar, K., and Watt, F.M. (2011). Reprogramming adult dermis to a neonatal state through epidermal activation of β-catenin. Development *138*, 5189–5199.

Dilão, R., Muraro, D., Nicolau, M., and Schoenauer, M. (2009). Validation of a Morphogenesis Model of Drosophila Early Development by a Multi-objective Evolutionary Optimization Algorithm. EvoBIO.

Dilão, R., and Muraro, D. (2010). A software tool to model genetic regulatory networks. Applications to the modeling of threshold phenomena and of spatial patterning in Drosophila. PLoS ONE *5*, e10743.

Dilão, R., and Sainhas, J. (2011). Validation and Calibration of Models for Reaction–Diffusion Systems. International Journal of Bifurcation and Chaos *08*, 1163–1182.

Donati, G., Proserpio, V., Lichtenberger, B.M., Natsuga, K., Sinclair, R., Fujiwara, H., and Watt, F.M. (2014). Epidermal Wnt/β-catenin signaling regulates adipocyte differentiation via secretion of adipogenic factors. Proc. Natl. Acad. Sci. U.S.a. *111*, E1501–E1509.

Donati, G., Rognoni, E., Hiratsuka, T., Liakath-Ali, K., Hoste, E., Kar, G., Kayikci, M., Russell, R., Kretzschmar, K., Mulder, K.W., et al. (2017). Wounding induces dedifferentiation of epidermal Gata6(+) cells and acquisition of stem cell properties. Nature Cell Biology *19*, 603–613.

Driskell, R.R., Jahoda, C.A.B., Chuong, C.-M., Watt, F.M., and Horsley, V. (2014). Defining dermal adipose tissue. Exp. Dermatol. *23*, 629–631.

Driskell, R.R., Lichtenberger, B.M., Hoste, E., Kretzschmar, K., Ben D Simons, Charalambous, M., Ferron, S.R., Herault, Y., Pavlovic, G., Ferguson-Smith, A.C., et al. (2013). Distinct fibroblast lineages determine dermal architecture in skin development and repair. Nature *504*, 277–281.

Eming, S.A., Martin, P., and Tomic-Canic, M. (2014). Wound repair and regeneration: mechanisms,

signaling, and translation. Science Translational Medicine *6*, 265sr6–265sr6.

Fuchs, E., and Horsley, V. (2008). More than one way to skin . . . Genes Dev. *22*, 976–985.

Hamilton, T.G., Klinghoffer, R.A., Corrin, P.D., and Soriano, P. (2003). Evolutionary divergence of platelet-derived growth factor alpha receptor signaling mechanisms. Mol. Cell. Biol. *23*, 4013–4025.

Hirashima, T., Rens, E.G., and Merks, R.M.H. (2017). Cellular Potts modeling of complex multicellular behaviors in tissue morphogenesis. Dev. Growth Differ. *59*, 329–339.

Hiratsuka, T., Fujita, Y., Naoki, H., Aoki, K., Kamioka, Y., and Matsuda, M. (2015). Intercellular propagation of extracellular signal-regulated kinase activation revealed by in vivo imaging of mouse skin. eLife *4*, e05178.

Hwang, J., San, B.H., Turner, N.J., White, L.J., Faulk, D.M., Badylak, S.F., Li, Y., and Yu, S.M. (2017). Molecular assessment of collagen denaturation in decellularized tissues using a collagen hybridizing peptide. Acta Biomater *53*, 268–278.

Jensen, K.B., Driskell, R.R., and Watt, F.M. (2010). Assaying proliferation and differentiation capacity of stem cells using disaggregated adult mouse epidermis. Nat Protoc *5*, 898–911.

Kawamoto, S., Niwa, H., Tashiro, F., Sano, S., Kondoh, G., Takeda, J., Tabayashi, K., and Miyazaki, J. (2000). A novel reporter mouse strain that expresses enhanced green fluorescent protein upon Cre-mediated recombination. FEBS Letters *470*, 263–268.

Lattouf, R., Younes, R., Lutomski, D., Naaman, N., Godeau, G., Senni, K., and Changotade, S. (2014). Picrosirius red staining: a useful tool to appraise collagen networks in normal and pathological tissues. J. Histochem. Cytochem. *62*, 751–758.

Lemons, J.M.S., Feng, X.-J., Bennett, B.D., Legesse-Miller, A., Johnson, E.L., Raitman, I., Pollina, E.A., Rabitz, H.A., Rabinowitz, J.D., and Coller, H.A. (2010). Quiescent Fibroblasts Exhibit High Metabolic Activity. PLoS Biol. *8*, e1000514.

Li, Y., Foss, C.A., Summerfield, D.D., Doyle, J.J., Torok, C.M., Dietz, H.C., Pomper, M.G., and Yu, S.M. (2012). Targeting collagen strands by photo-triggered triple-helix hybridization. Proc. Natl. Acad. Sci. U.S.a. *109*, 14767–14772.

Lichtenberger, B.M., Mastrogiannaki, M., and Watt, F.M. (2016). Epidermal β-catenin activation remodels the dermis via paracrine signalling to distinct fibroblast lineages. Nat Commun *7*, 10537.

Mort, R.L., Ford, M.J., Sakaue-Sawano, A., Lindstrom, N.O., Casadio, A., Douglas, A.T., Keighren, M.A., Hohenstein, P., Miyawaki, A., and Jackson, I.J. (2014). Fucci2a: A bicistronic cell cycle reporter that allows Cre mediated tissue specific expression in mice. Cell Cycle *13*, 2681–2696.

Muraro, D., and Dilão, R. (2013). A parallel multi-objective optimization algorithm for the calibration of mathematical models. Swarm and Evolutionary Computation *8*, 13–25.

Page, M.E., Lombard, P., Ng, F., Göttgens, B., and Jensen, K.B. (2013). The epidermis comprises autonomous compartments maintained by distinct stem cell populations. Cell Stem Cell *13*, 471–482.

Park, S., Gonzalez, D.G., Guirao, B., Boucher, J.D., Cockburn, K., Marsh, E.D., Mesa, K.R., Brown, S., Rompolas, P., Haberman, A.M., et al. (2017). Tissue-scale coordination of cellular behaviour promotes epidermal wound repair in live mice. Nature Cell Biology *19*, 155–163.

Plikus, M.V., Guerrero-Juarez, C.F., Ito, M., Li, Y.R., Dedhia, P.H., Zheng, Y., Shao, M., Gay, D.L., Ramos, R., His, T.-C., et al. (2017). Regeneration of fat cells from myofibroblasts during wound healing. Science aai8792.

Robertson, E.J., Charatsi, I., Joyner, C.J., Koonce, C.H., Morgan, M., Islam, A., Paterson, C., Lejsek, E., Arnold, S.J., Kallies, A., et al. (2007). Blimp1 regulates development of the posterior forelimb, caudal pharyngeal arches, heart and sensory vibrissae in mice. Development *134*, 4335–4345.

Rognoni, E., Gomez, C., Pisco, A.O., Rawlins, E.L., Simons, B.D., Watt, F.M., and Driskell, R.R. (2016). Inhibition of β-catenin signalling in dermal fibroblasts enhances hair follicle regeneration during wound healing. Development dev.131797.

Sang, L., and Coller, H.A. (2009a). Fear of commitment: Hes1 protects quiescent fibroblasts from irreversible cellular fates. Cell Cycle *8*, 2161–2167.

Sang, L., and Coller, H.A. (2009b). Fear of commitment. Cell Cycle 1–7.

Shaw, T.J., and Martin, P. (2016). Wound repair: a showcase for cell plasticity and migration. Current Opinion in Cell Biology *42*, 29–37.

Snippert, H.J., van der Flier, L.G., Sato, T., van Es, J.H., van den Born, M., Kroon-Veenboer, C., Barker, N., Klein, A.M., van Rheenen, J., Simons, B.D., et al. (2010). Intestinal Crypt Homeostasis Results from Neutral Competition between Symmetrically Dividing Lgr5 Stem Cells. Cell *143*, 134–144.

Suh, E.J., Remillard, M.Y., Legesse-Miller, A., Johnson, E.L., Lemons, J.M.S., Chapman, T.R., Forman, J.J., Kojima, M., Silberman, E.S., and Coller, H.A. (2012). A microRNA network regulates proliferative timing and extracellular matrix synthesis during cellular quiescence in fibroblasts. Genome Biol. *13*, R121.

Swat, M.H., Thomas, G.L., Belmonte, J.M., Shirinifard, A., Hmeljak, D., and Glazier, J.A. (2012). Multi-scale modeling of tissues using CompuCell3D. Methods Cell Biol. *110*, 325–366.

Telerman, S.B., Rognoni, E., Sequeira, I., Pisco, A.O., Lichtenberger, B.M., Culley, O., Viswanathan, P., Driskell, R.R., and Watt, F.M. (2017). Dermal Blimp1 acts downstream of epidermal TGFβ and Wnt/β-catenin to regulate hair follicle formation and growth. J. Invest. Dermatol.

van Deursen, J.M. (2014). The role of senescent cells in ageing. Nature *509*, 439–446.

Watt, F.M. (2014). Mammalian skin cell biology: at the interface between laboratory and clinic. Science *346*, 937–940.

Rognoni, Pisco et al, Fig 1

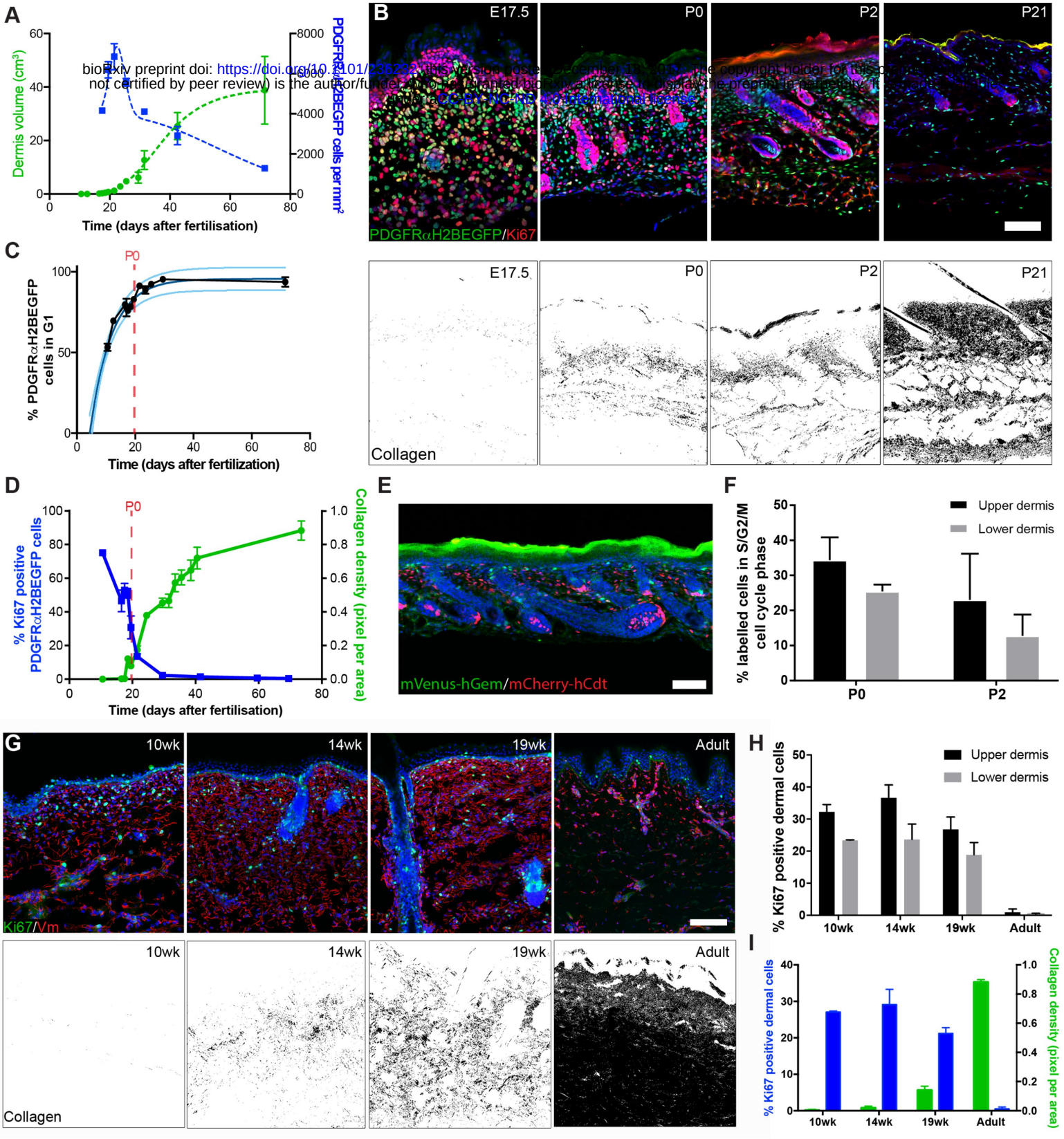

Rognoni, Pisco et al, Fig 2

A

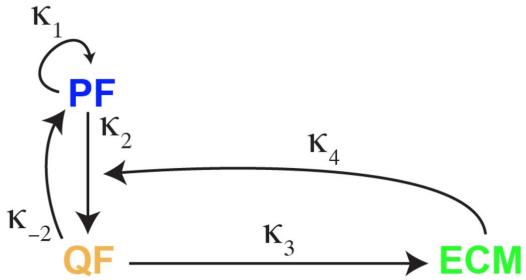

B

$$\begin{cases} \frac{d\mathrm{PF}}{dt} = \beta \mathrm{PF} + k_{-2}\mathrm{QF} - k_4 \mathrm{ECM}\,\mathrm{PF} \\ \frac{d\mathrm{QF}}{dt} = k_2 \mathrm{PF} - k_{-2}\mathrm{QF} + k_4 \mathrm{ECM}\,\mathrm{PF} - k_6 \mathrm{QF} \\ \frac{d\mathrm{ECM}}{dt} = k_3 \mathrm{QF} - k_7 \mathrm{ECM} \end{cases}$$

C

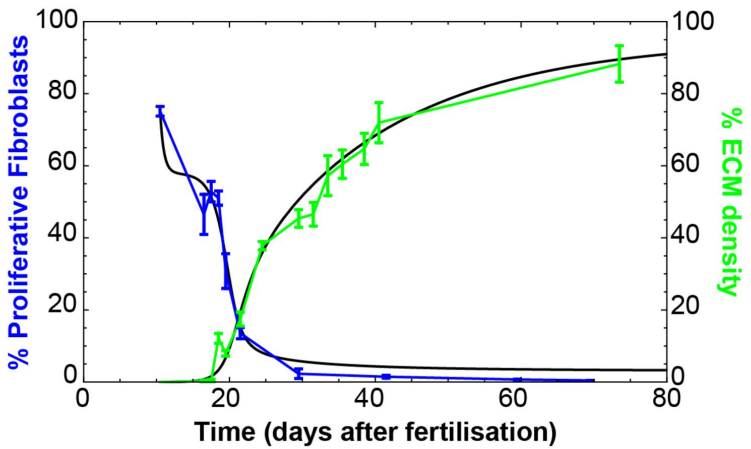

Rognoni, Pisco et al, Fig 3

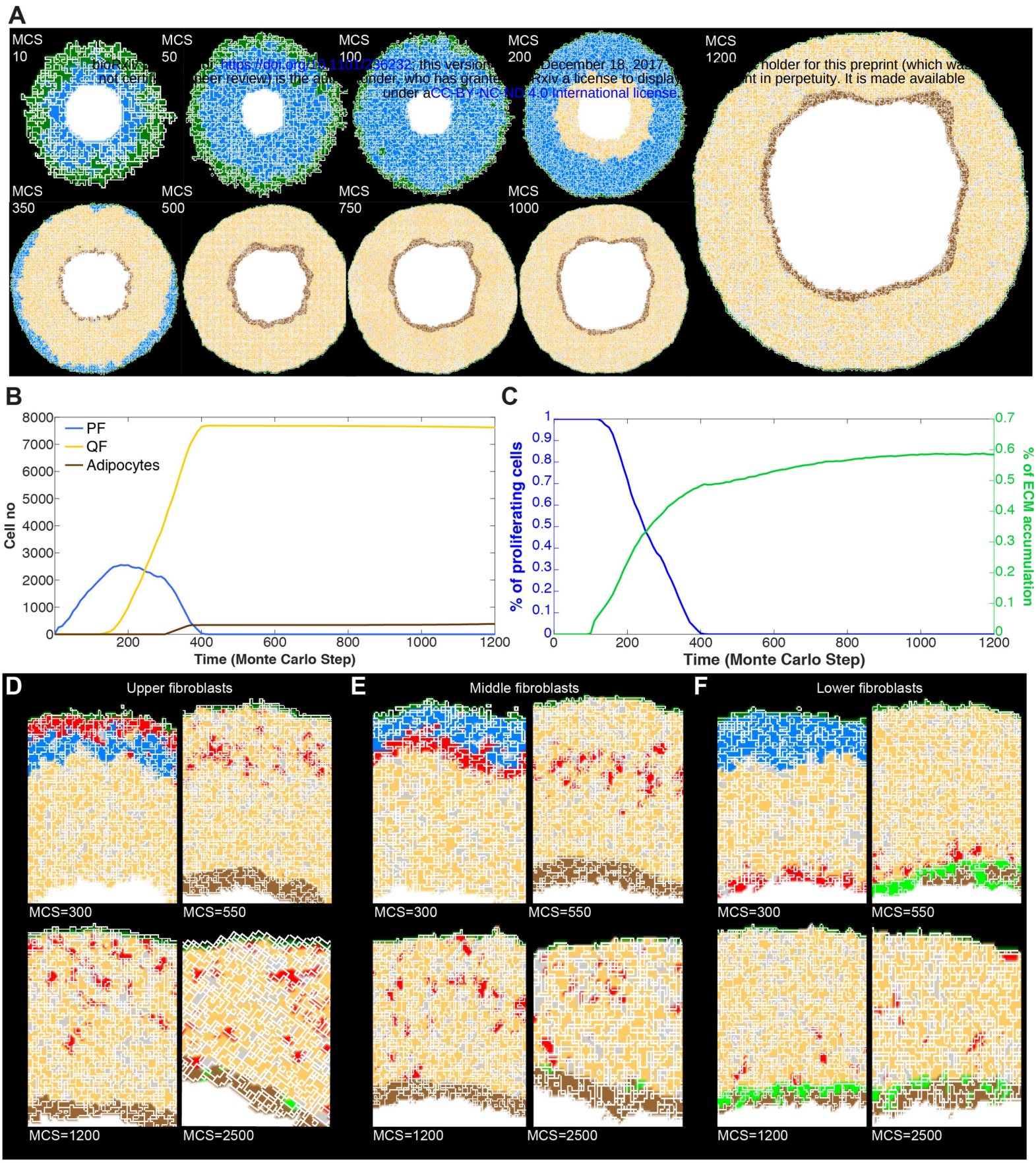

Rognoni, Pisco et al, Fig 4

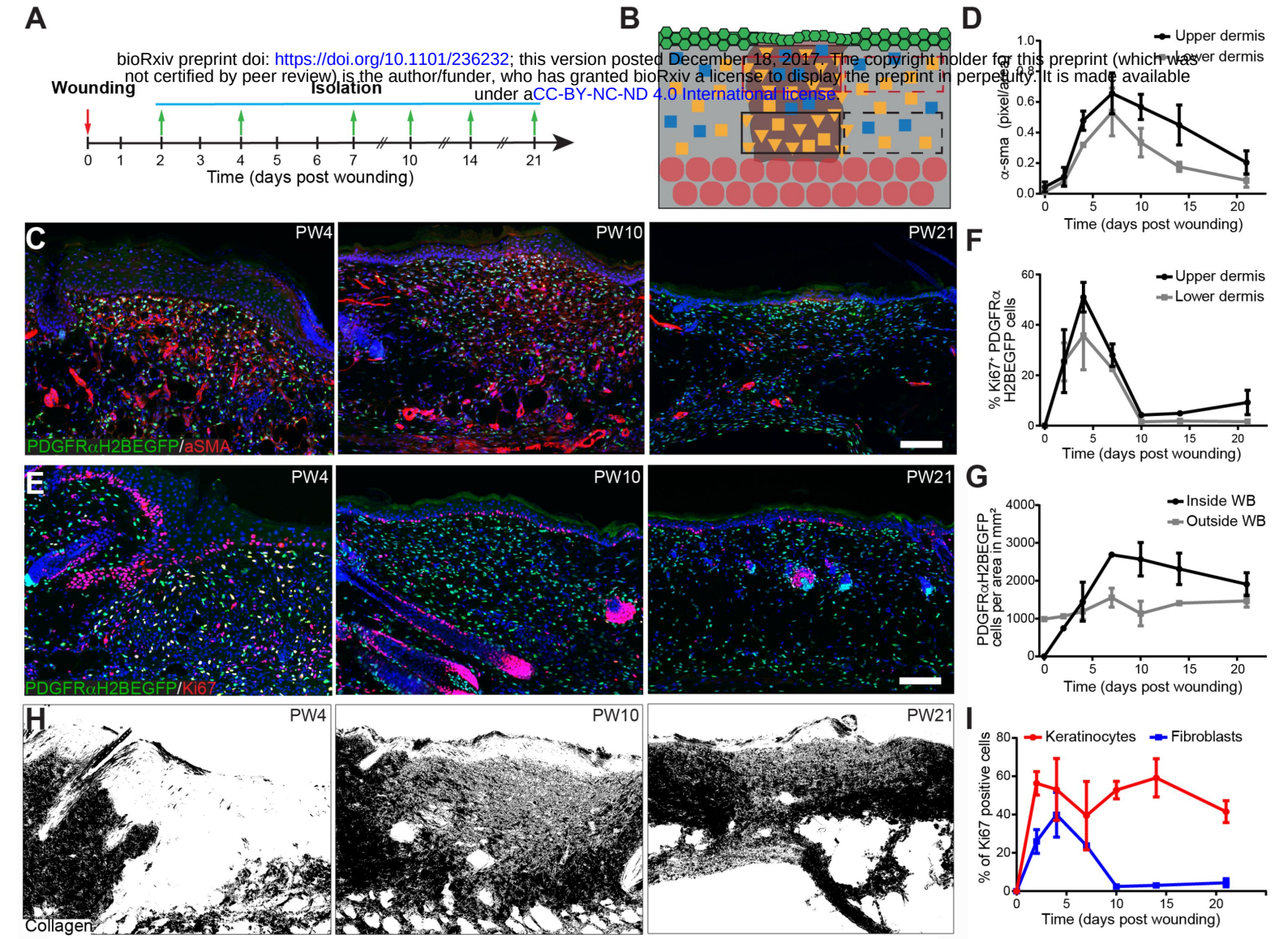

Rognoni, Pisco et al, Fig 5

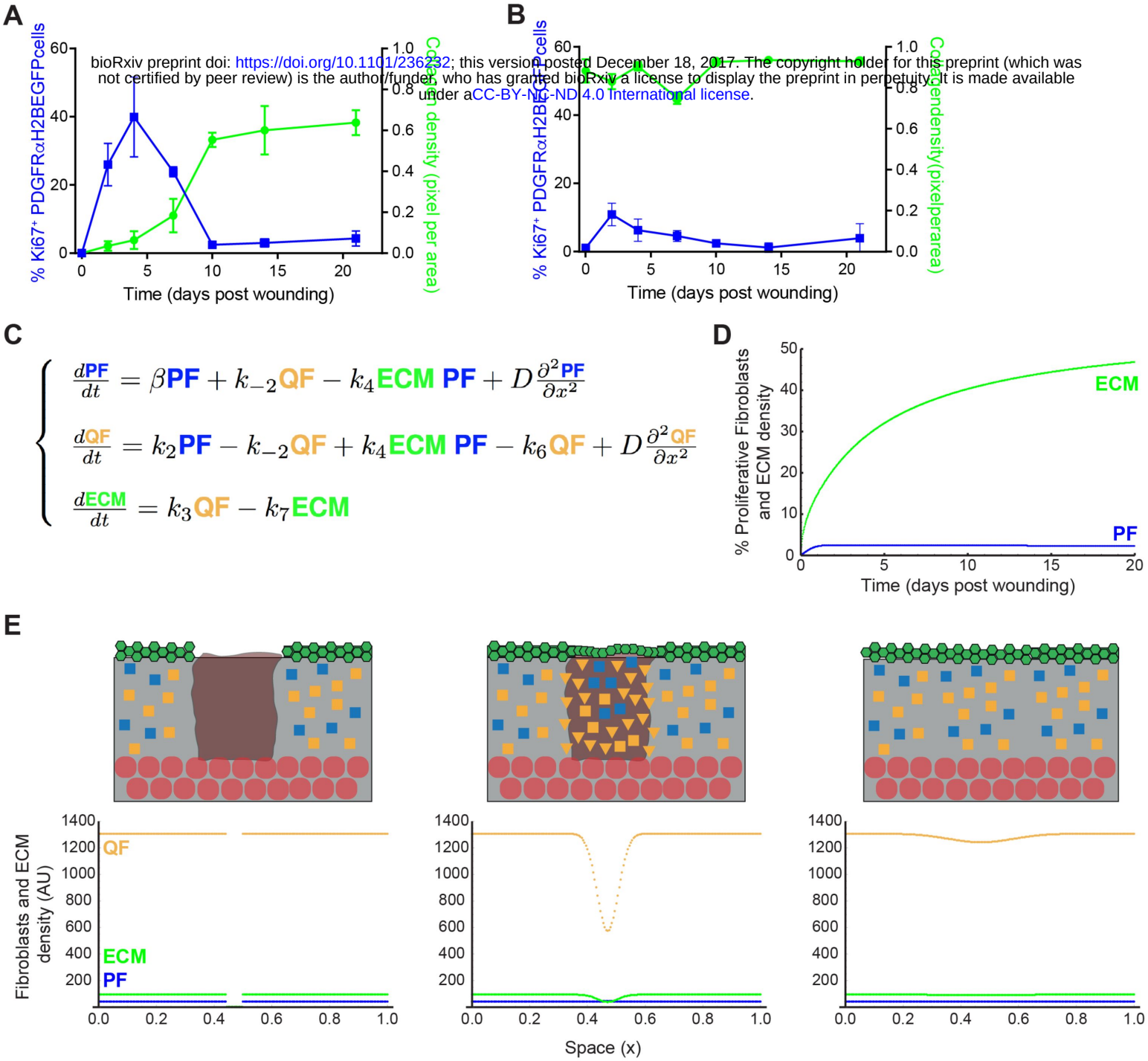

Rognoni, Pisco et al, Fig 6

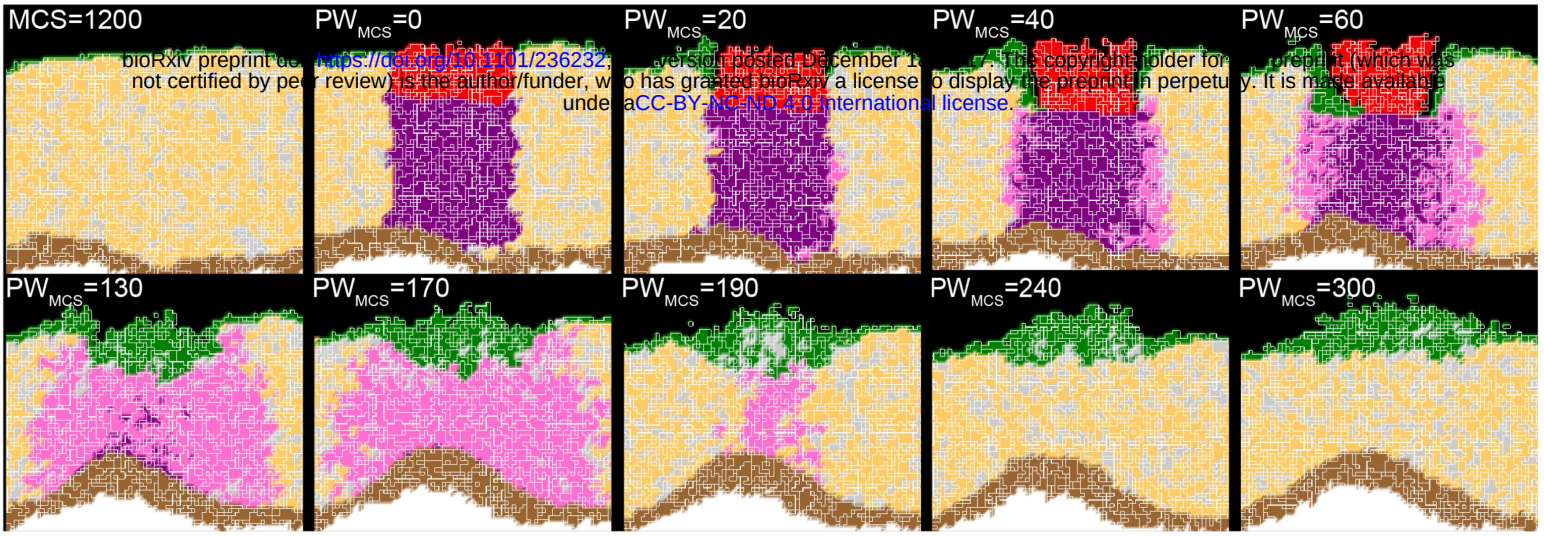

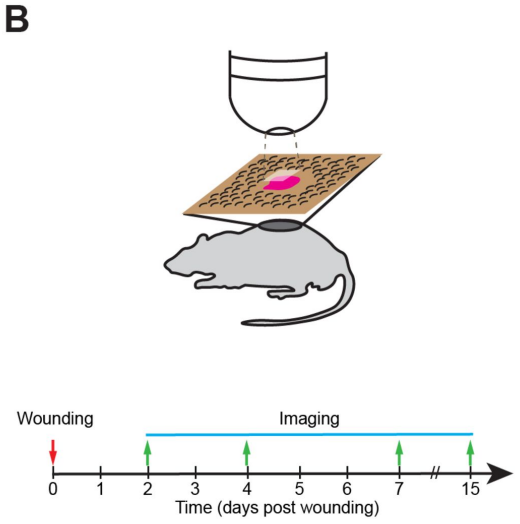

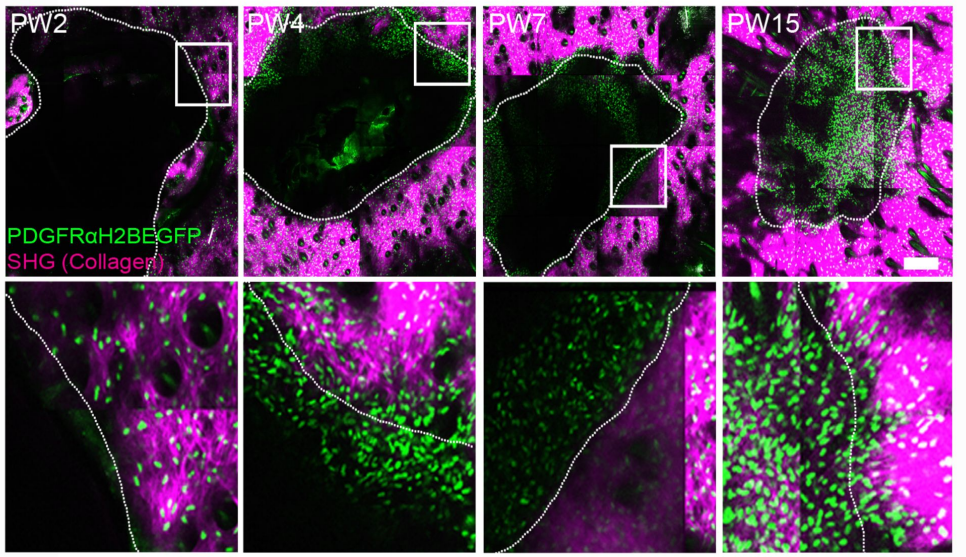

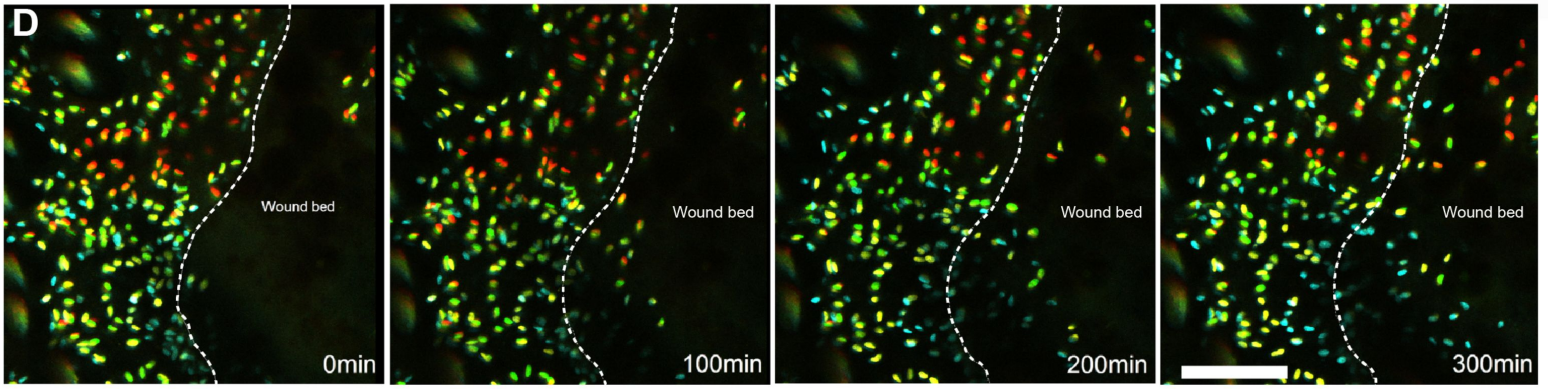

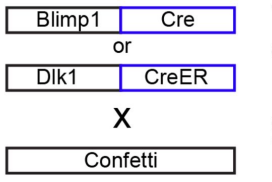

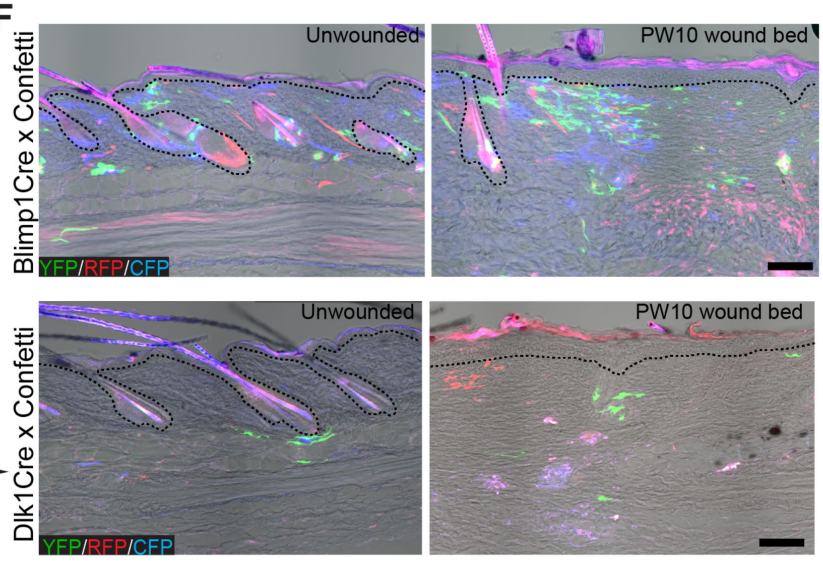

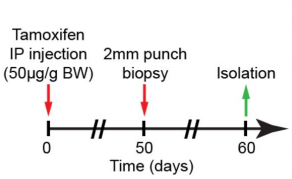

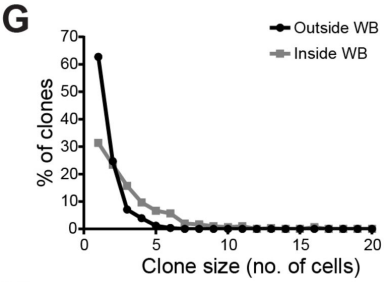

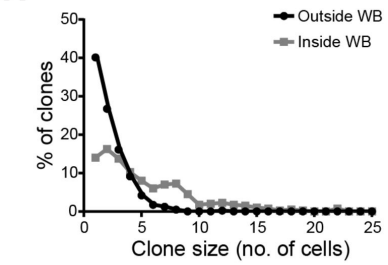

Rognoni, Pisco et al, Fig 7

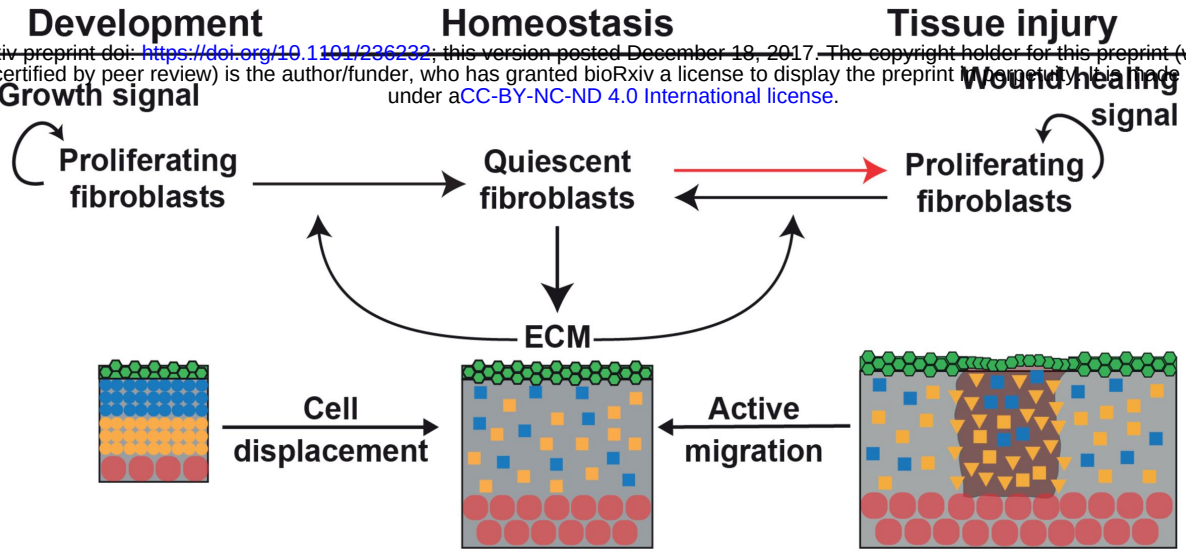

Rognoni, Pisco et al, Fig EV1 (related to Fig 1)

A

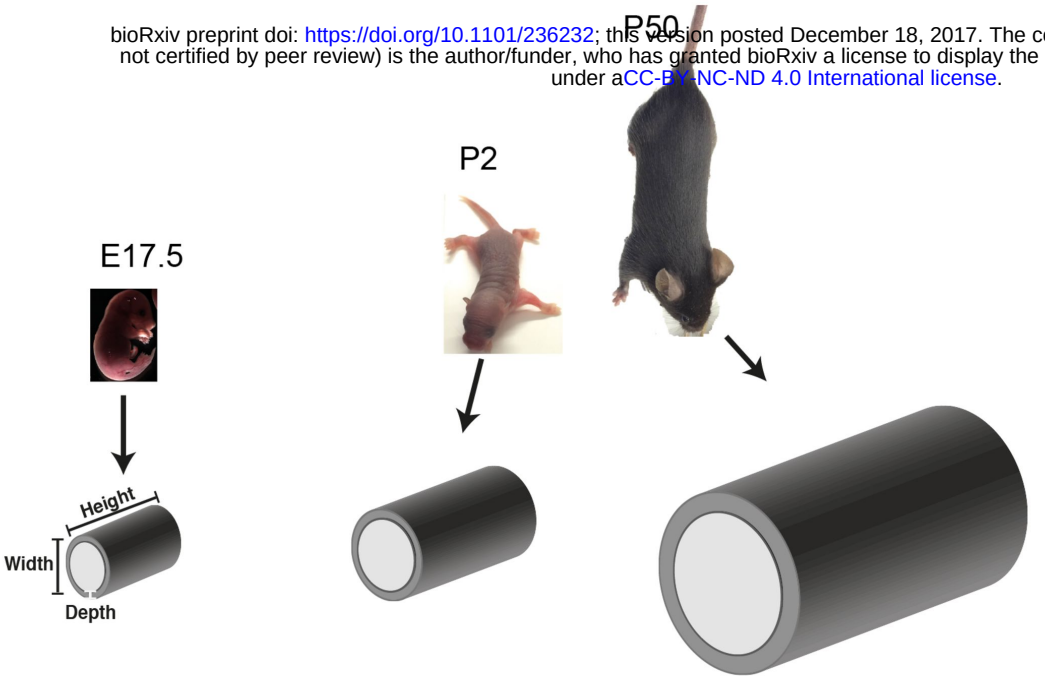

$N_E \sim d_{E17.5} \times dv_{E17.5}$ $N_N \sim d_{P2} \times dv_{P2}$ $N_A \sim d_{P50} \times dv_{P50}$

From E17.5 to P2:
Dermis volume 7x
Cell count 10x
} ~1:1

From P2 to P50:
Dermis volume 13x
Cell count 3x
} ~1:4

Estimated cell divisions E17.5 to P2:

$N_N = N_E \times 2^n$

$n = \log_2 \frac{N_N}{N_E}$

$n = 3.4$

➤**Expansion through proliferation**

Estimated cell divisions P2 to P50:

$N_A = N_N \times 2^n$

$n = \log_2 \frac{N_A}{N_N}$

$n = 1.3$

➤**Expansion through ECM production**

B

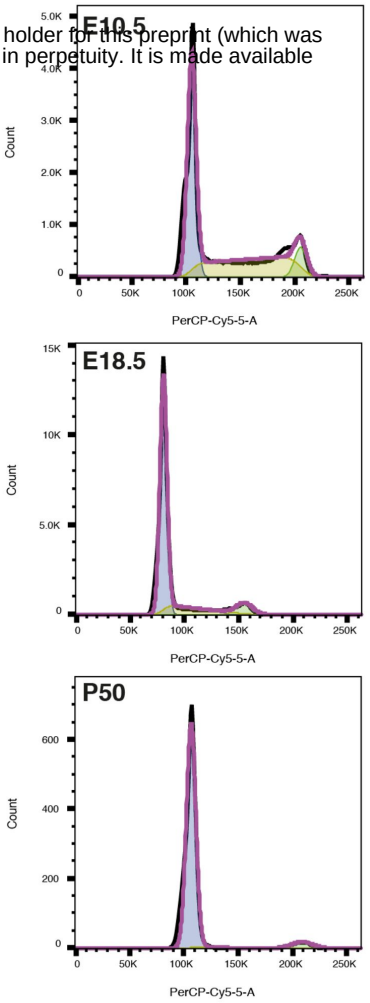

C

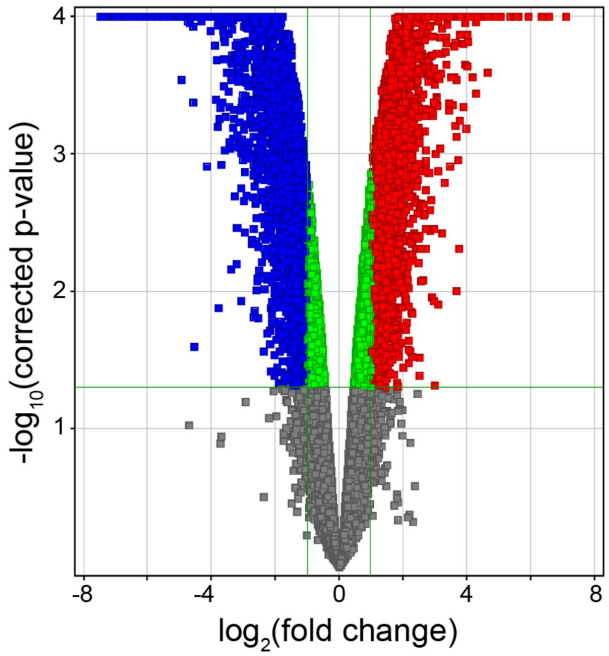

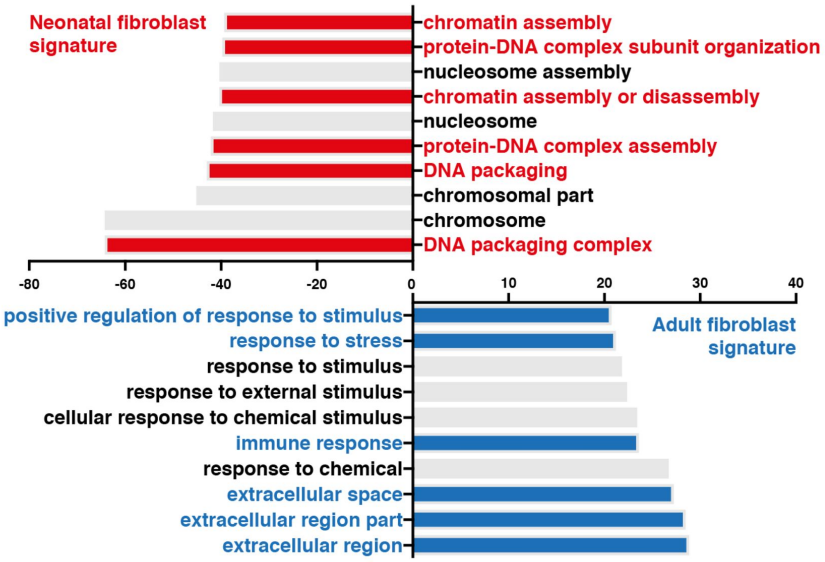

Rognoni, Pisco et al, Figure EV2 (related to Fig 1)

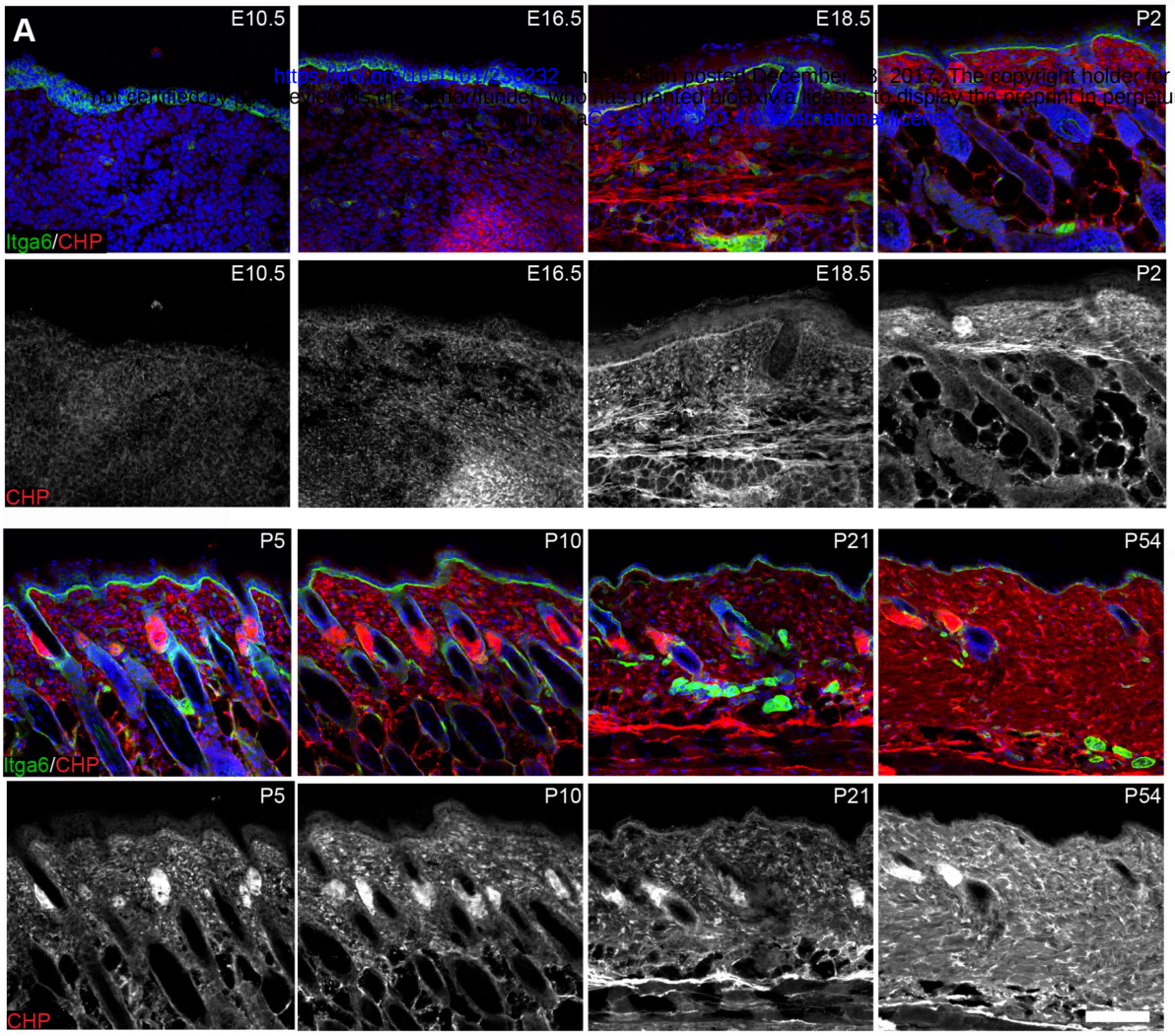

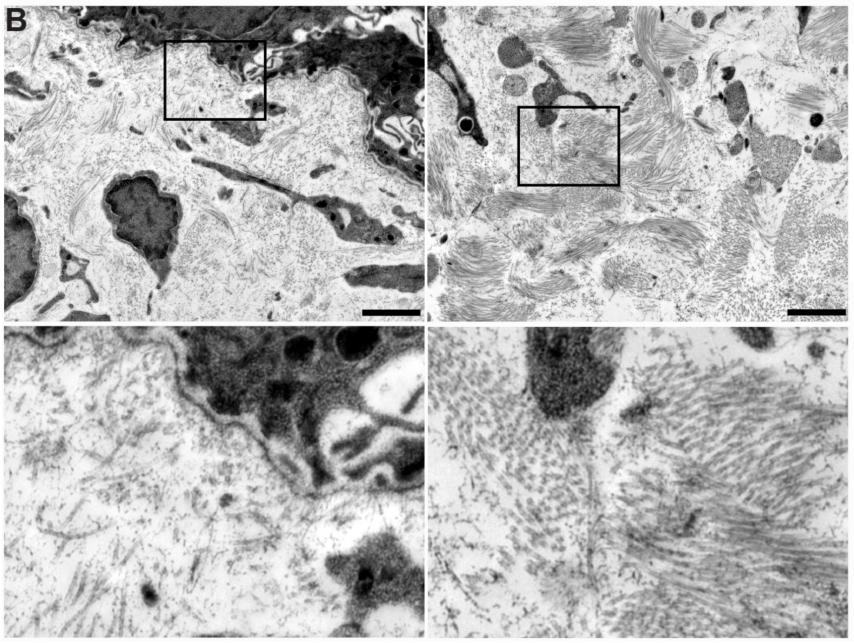

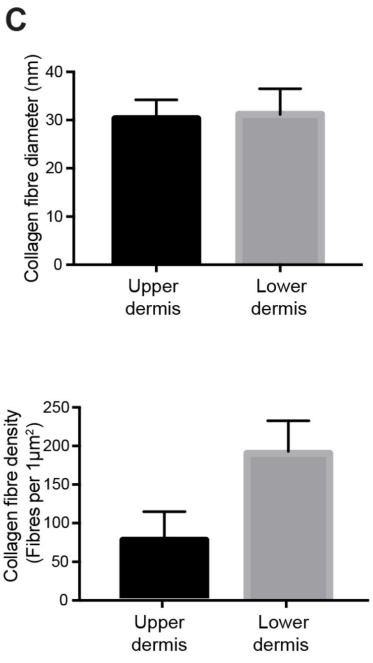

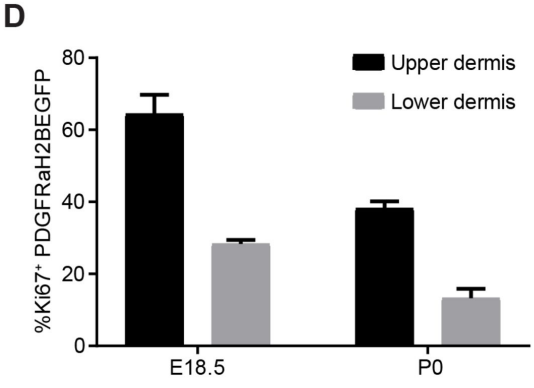

Rognoni, Pisco et al, Fig EV3 (related to Fig 3)

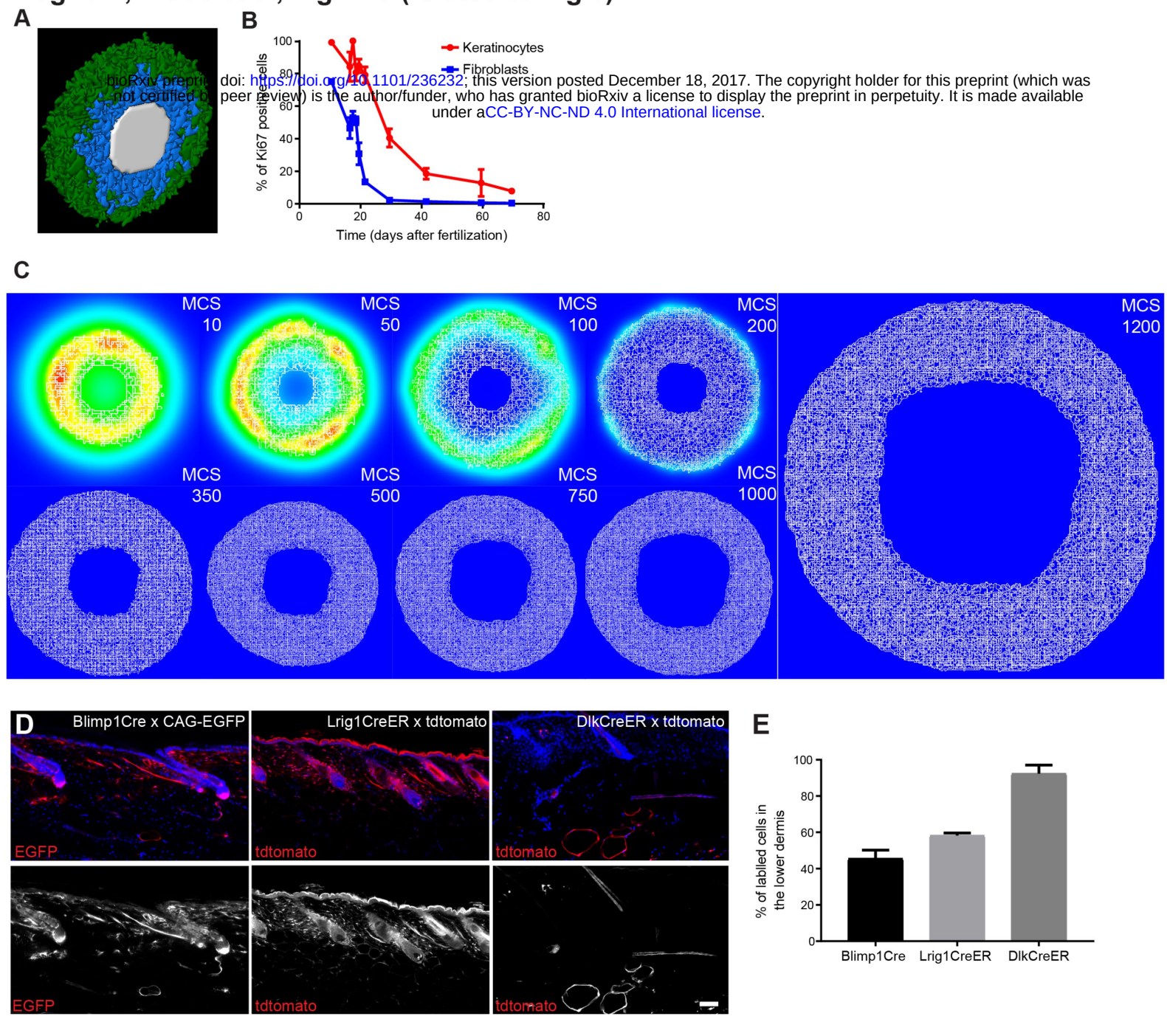

Rognoni, Pisco et al, Fig EV4 (related to Fig 4)

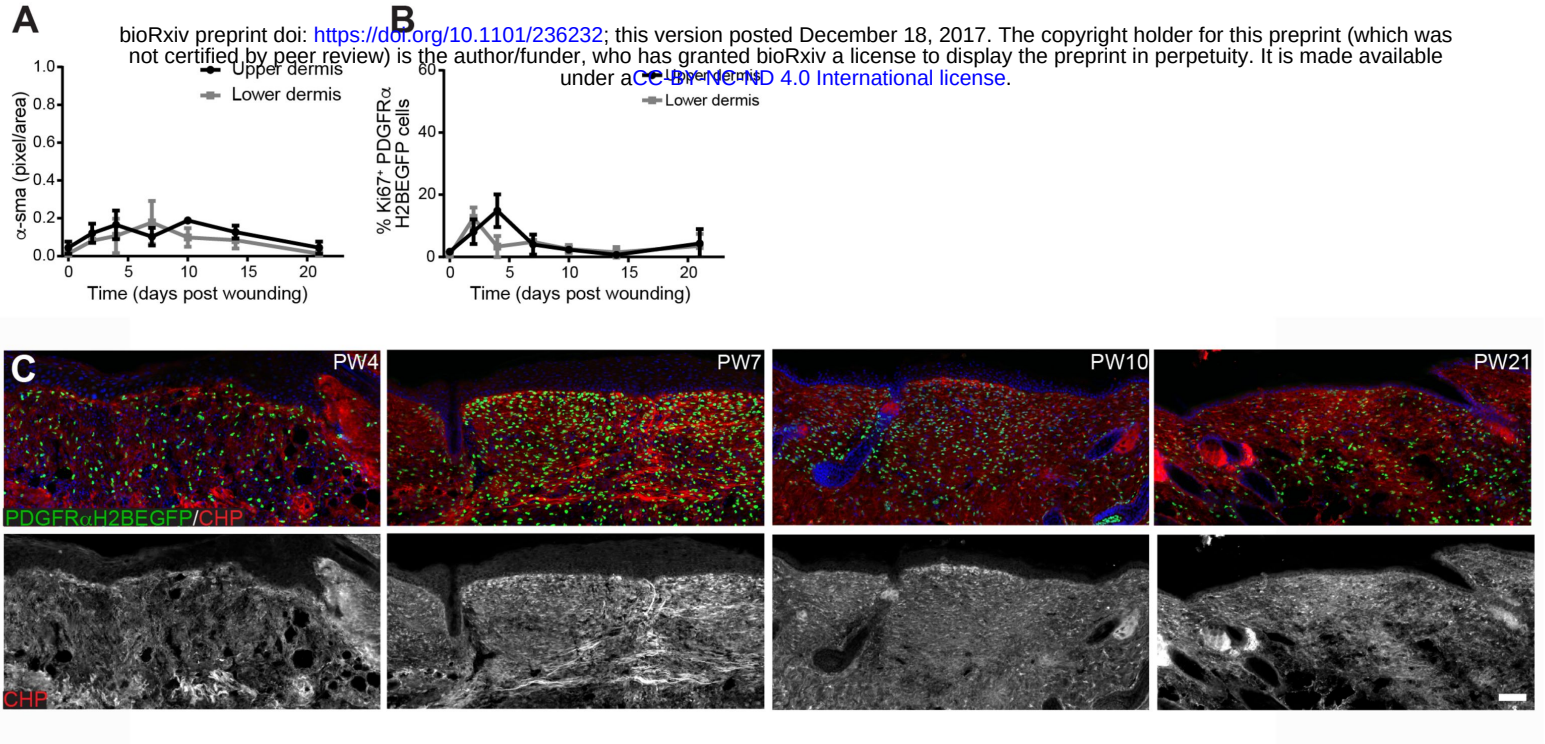

Rognoni, Pisco et al, Fig EV5 (related to Fig 6)

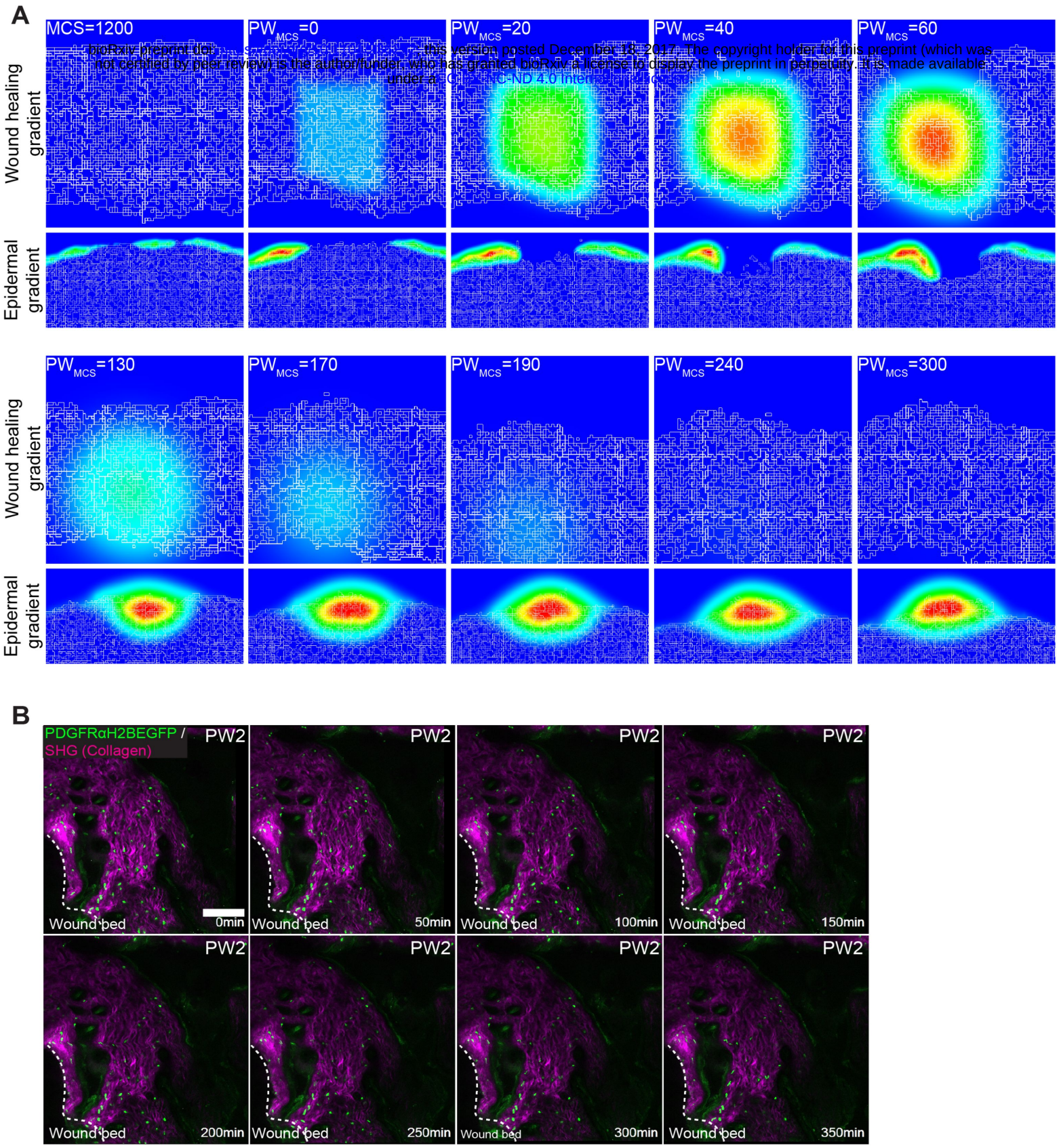

Rognoni, Pisco et al, Fig EV6 (related to Fig 6)

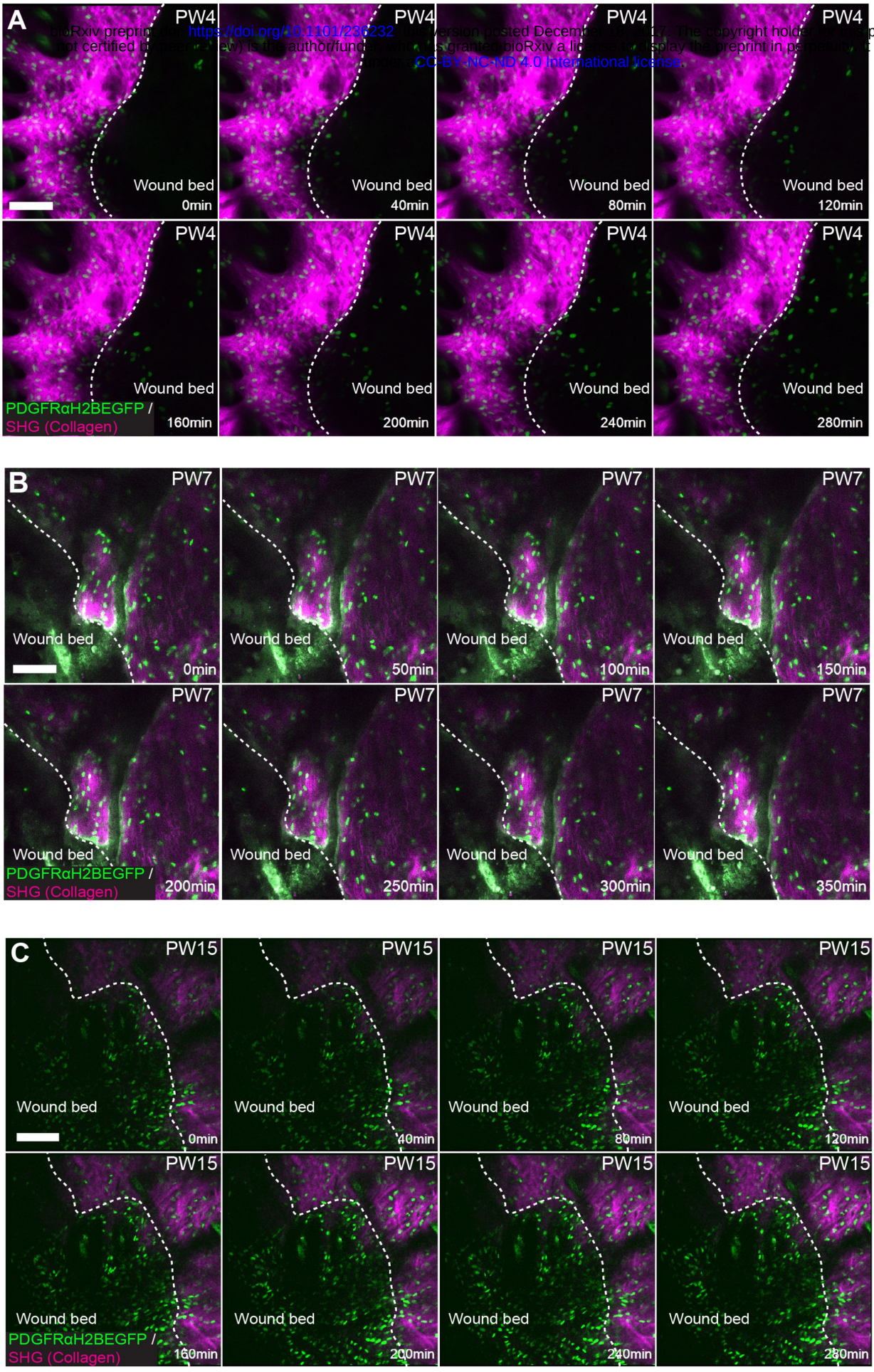

Table EV1
This table refers to Fig 1 and Fig EV1

Figure 1A Volume Measurements

E10.5

Replicates	Length (cm)	Diameter (cm)	Body Volume (cm3)
1	0.63	0.15	0.01
2	0.64	0.15	0.01
3	0.52	0.17	0.01
4	0.45	0.15	0.01
5	0.75	0.16	0.01
6	0.68	0.14	0.01
7	0.77	0.17	0.02
8	0.65	0.14	0.01
9	0.70	0.13	0.01
10	0.75	0.14	0.01
11	0.68	0.15	0.01

E12.5

Replicates	Length (cm)	Diameter (cm)	Body Volume (cm3)
1	0.55	0.23	0.02
2	0.49	0.24	0.02
3	0.46	0.20	0.01
4	0.52	0.24	0.02
5	0.50	0.19	0.01
6	0.53	0.20	0.02
7	0.49	0.19	0.01

E16.5

Replicates	Length (cm)	Diameter (cm)	Body Volume (cm3)
1	1.00	0.42	0.14
2	1.10	0.38	0.12
3	1.10	0.44	0.17
4	1.10	0.49	0.21
5	0.99	0.49	0.19
6	1.10	0.54	0.25
7	1.25	0.45	0.20
8	1.00	0.44	0.15
9	1.20	0.54	0.27

E17.5

Replicates	Length (cm)	Diameter (cm)	Body Volume (cm3)
1	1.10	0.50	0.22
2	1.10	0.50	0.22
3	1.00	0.60	0.28
4	1.30	0.50	0.26
5	1.00	0.60	0.28
6	0.90	0.50	0.18
7	1.30	0.60	0.37
8	1.00	0.50	0.20
9	1.10	0.60	0.31

E18.5

Replicates	Length (cm)	Diameter (cm)	Body Volume (cm3)

P0

Replicates	Length (cm)	Diameter (cm)	Body Volume (cm3)

1	1.60	0.80	0.80
2	1.70	0.70	0.65
3	1.60	0.65	0.53
4	1.80	0.60	0.51
5	1.70	0.60	0.48
6	1.50	0.60	0.42
7	1.60	0.60	0.45
8	1.40	0.50	0.27
9	1.50	0.60	0.42
10	1.50	0.60	0.42
11	1.60	0.60	0.45
12	1.60	0.55	0.38

1	1.70	0.90	1.08
2	1.80	0.60	0.51
3	1.80	0.80	0.90
4	1.80	0.70	0.69
5	1.90	0.80	0.96
6	1.80	0.70	0.69
7	1.60	0.70	0.62
8	1.70	0.70	0.65

P2

Replicates	Length (cm)	Diameter (cm)	Body Volume (cm3)
1	2.00	0.90	1.27
2	2.00	0.90	1.27
3	2.00	1.00	1.57
4	2.20	1.00	1.73
5	2.10	0.90	1.34
6	1.80	0.80	0.90
7	2.00	0.80	1.01
8	1.80	0.80	0.90
9	2.30	0.90	1.46
10	2.10	0.90	1.34
11	1.80	0.80	0.90
12	1.80	0.80	0.90

P4

Replicates	Length (cm)	Diameter (cm)	Body Volume (cm3)
1	2.80	1.20	3.17
2	2.50	1.20	2.83
3	2.60	1.00	2.04
4	2.70	1.30	3.58
5	2.70	1.10	2.57
6	2.60	1.20	2.94
7	2.50	1.10	2.38
8	3.00	1.10	2.85
9	2.80	1.20	3.17

P6

Replicates	Length (cm)	Diameter (cm)	Body Volume (cm3)
1	3.20	1.40	4.93
2	3.30	1.30	4.38

P10

Replicates	Length (cm)	Diameter (cm)	Body Volume (cm3)
1	3.80	1.80	9.67
2	4.00	1.80	10.18

3	3.10	1.30	4.11	1	3.50	1.50	6.19
4	3.20	1.20	3.62	2	3.30	1.30	4.38
5	3.20	1.40	4.93	3	3.40	1.40	5.23
6	3.30	1.40	5.08	4	3.20	1.30	4.25
7	3.30	1.50	5.83	5	3.60	1.40	5.54
8	3.40	1.40	5.23	6	3.10	1.50	5.48
				7	3.40	1.40	5.23
				8	3.40	1.40	5.23

P21

Male replicates	Length (cm)	Diameter (cm)	Body Volume (cm3)	Female replicates	Length (cm)	Diameter (cm)	Body Volume (cm3)
1	5	2.1	17.3180295	1	4.8	1.8	12.21451224
2	5.2	2.1	18.01075068	2	5	2	15.70796327
3	5	2	15.70796327	3	4.4	1.8	11.19663622
4	4.6	2	14.45132621	4	4.5	1.8	11.45110522
5	5	2.1	17.3180295	5	4.2	1.6	8.444601053
6	4.5	2	14.13716694	6	4.2	1.6	8.444601053
7	4.8	2.2	18.24637013	7	4	1.7	9.079202769
8	4.6	1.9	13.0423219	8	4.1	1.7	9.306182838
9	4.8	1.8	12.21451224				
10	4.2	1.8	10.68769821				
11	3.9	1.6	7.841415263				
12	4.4	1.6	8.846724913				

P38

Male replicates	Length (cm)	Diameter (cm)	Body Volume (cm3)	Female replicates	Length (cm)	Diameter (cm)	Body Volume (cm3)
1	5.5	2.8	33.86636881	1	5.8	2.5	28.47068342
2	5.8	2.6	30.79389119	2	5.6	2.2	21.28743182
3	5.6	2.6	29.73203287	3	5.3	2.2	20.14703369
4	5.7	2.5	27.97980957	4	5.2	2	16.3362818

5	5	2.4	22.61946711
6	5.4	2.3	22.43568394
7	5.5	2.5	26.99806187
8	4.9	2.5	24.05281875

P50

Male replicates	Length (cm)	Diameter (cm)	Body Volume (cm3)	Female replicates	Length (cm)	Diameter (cm)	Body Volume (cm3)
1	7	2.6	37.16504109	1	6.2	2.4	28.04813921
2	7.5	2.8	46.18141201	2	6.3	2.7	36.07098145
3	6.5	3	45.94579256	3	6.5	3	45.94579256
4	7.3	3.4	66.27818021	4	5.8	2.30	24.09758645
5	6.8	2.40	30.76247526	5	5.6	2.5	27.48893572

Figure S1A
Ratio calculations

	E17.5	P2	P50
Average body volume (cm3)	0.26	1.22	38.80
Average dermis depth (cm)	0.02	0.03	0.04
Average dermis volume (cm3)	0.03	0.18	2.32
Average fibroblast density	4156.94	6841.76	1282.64

	P2 - E17.5	P50 - P2
Ratio body volume	4.75	31.88
Ratio dermis volume	6.52	13.25
Ratio cell number	10.73	2.48
Predicted number of cell divisions	3.4241261	1.31243661

Mathematical derivation of the negative feedback loop model

1 Dermis maturation

We set to mechanistically understand the process whereby fibroblasts orchestrates dermal maturation and wound healing. It is well established that during embryonic developmental stages (E) mouse fibroblasts proliferate and this process is driven by the presence of growth factors[1], which here we designate by GF.

Driskell et al[2] showed that around E16.5 the multi-potent fibroblasts start maturing, giving rise to the two fibroblasts lineages, papillary and reticular. As both papillary and reticular fibroblasts are proliferative cells, for modelling simplification purposes, we combined the two lineages in a global proliferating fibroblasts (PF) term. During development, PF is progressively arrested at the G1 phase of the cell cycle and, in our model, we designate these arrested cells by quiescent fibroblasts (QF). While both PF and QF are associated with the metabolism of the dermis, QF are more efficient at depositing extracellular matrix (ECM) and PF cells' main function is proliferation. This difference is the basis of the essential architecture of the dermis.

As observed in Figure 1D, the increase in the amount of ECM is accompanied by a decrease in the number of PF, suggesting that ECM has a repressive effect over PF. We therefore assume that the reduction in PF by the presence of ECM can be described by a negative feedback mechanism of the following form

$$\text{PF} + \text{ECM} \longrightarrow \text{QF} + \text{ECM} \tag{1}$$

This is a catalytic mechanism, in which the presence of ECM enhances the entry into quiescence of proliferating cells via a cell-to-matrix interaction[3]. All the processes described are summarised in the regulatory diagram shown in Figure 2A and the kinetic diagrams describing the regulatory diagram are:

$$\begin{cases} \text{GF} + \text{PF} \xrightarrow{k_1} 2\text{PF} \\ \text{PF} \underset{k_{-2}}{\overset{k_2}{\rightleftharpoons}} \text{QF} \\ \text{QF} \xrightarrow{k_3} \text{QF} + \text{ECM} \\ \boxed{\text{PF} + \text{ECM} \xrightarrow{k_4} \text{QF} + \text{ECM}} \\ \text{PF} \xrightarrow{k_5} \emptyset \\ \text{QF} \xrightarrow{k_6} \emptyset \\ \text{ECM} \xrightarrow{k_7} \emptyset \end{cases} \tag{2}$$

As usual, rate constants k_i are non-negative. The box in system (2) highlights the mechanism whereby the presence of ECM manifests as a negative feedback loop, promoting the transition between PF and QF.

We will first describe the behaviour of PF and ECM during the whole dermal maturation. We start by assuming that during the first stage of the embryonic development the growth factor GF is not a limiting factor. The mechanism outlined by the kinetic diagrams (2) is described by the following system of equations:

$$\begin{cases} \frac{dPF}{dt} = k_1 GF\ PF - \ k_2 PF + k_{-2} QF - k_4 ECM\ PF - \ k_5 PF \\ \frac{dQF}{dt} = k_2 PF - k_{-2} QF + k_4 ECM\ PF - k_6 QF \\ \frac{dECM}{dt} = k_3 QF - k_7 ECM \end{cases} \tag{3}$$

For simplification, PF, QF and ECM denote amounts of either cells or proteins. With the new constant

$$\beta = k_1 GF - k_2 - k_5, \tag{4}$$

the system of equations (3) simplifies to

$$\begin{cases} \frac{dPF}{dt} = \beta PF + k_{-2}QF - k_4 ECM\ PF \\ \frac{dQF}{dt} = k_2 PF - k_{-2}QF + k_4 ECM\ PF - k_6 QF \\ \frac{dECM}{dt} = k_3 QF - k_7 ECM \end{cases} \tag{5}$$

The system of equations (5) is our proposed mathematical model for the maturation process of the dermis.

The system of equations (5) has a fixed point other than the trivial solution:

$$\begin{cases} PF^* = \frac{k_7(k_{-2}(\beta+k_2)+\beta k_6)}{k_3 k_4(\beta+k_2)} \\ QF^* = \frac{k_7(k_{-2}(\beta+k_2)+\beta k_6)}{k_3 k_4 k_6} \\ ECM^* = \frac{k_{-2}(\beta+k_2)+\beta k_6}{k_4 k_6} \end{cases} \tag{6}$$

The stability of the steady state (6) can be analysed through the Jacobian matrix of (5), calculated at the fixed point (6). The Jacobian matrix is given by

$$\mathcal{J} = \begin{pmatrix} \beta - \frac{k_{-2}(\beta+k_2)+\beta k_6}{k_6} & k_{-2} & -\frac{(k_{-2}(\beta+k_2)+\beta k_6)k_7}{(\beta+k_2)k_3} \\ k_2 + \frac{k_{-2}(\beta+k_2)+\beta k_6}{k_6} & -k_{-2} - k_6 & \frac{(k_{-2}(\beta+k_2)+\beta k_6)k_7}{(\beta+k_2)k_3} \\ 0 & k_3 & -k_7 \end{pmatrix} \tag{7}$$

If all the eigenvalues of the Jacobian matrix (7) have negative real parts, the fixed point (6) is stable, leading to a steady dermis structure. We will use this to constrain the fitting of the model parameters to the experimental data, as our goal now is to obtain the parameters that offer the best fit. The kinetic model described by the system of equations (5) and by the regulatory mechanism depicted in (2) depends on seven independent parameters, with different ranges, and three initial conditions.

We have two independent experimental datasets that we must fit. Table 1 contains the quantification of the amount of proliferating fibroblasts, as a percentage of the total number of fibroblasts, during mouse development. Table 2 contains the quantification of the total amount of collagen, as measured by Picrosirius red staining, with age.

Table 1: Temporal changes in fibroblast proliferation.

Time (days)	PF (%)	Standard deviation
10.5	75.1	1.4
16.5	46.5	6.4
17.5	52.8	2.8
18.5	51.0	2.0
19.5	30.8	4.8
21.5	13.5	1.6
29.5	2.3	1.4
41.5	1.5	0.4
59.5	0.69	0.1
69.5	0.44	0.04

Table 2: Experimental data for ECM.

Time (days)	ECM (%)	Standard deviation
10.5	0	0
16.5	0.3	0.2
17.5	0.4	0.4
18.5	12.1	1.4
19.5	7.9	0.8
21.5	17.4	1.9
24.5	37.8	1.1
29.5	45.4	2.4
31.5	46.5	3.3
33.5	57.2	4.5
35.5	60.4	3.9
38.5	64.7	4.3
40.5	72.0	5.6
73.5	88.3	5.1

To fit the experimental data in Tables 1 and 2 with the the model equations (5), and due to the large number of free parameters, we follow a Monte Carlo technique adapted to the particularity of having two data sets to fit. In this multi-objective optimisation problem, we are in the context of a Pareto optimisation problem, which implies that there are no unique solutions[4,5]. To implement the Pareto optimisation procedure, we calculated the mean square deviations of the two data sets, for each set of parameter values, and chose a solution on the Pareto front of the multi-objective optimisation problem. Any solution belonging to the Pareto front is a minimal Pareto solution, in the sense that the value of one objective cannot be improved without degrading the value of the other objective[4,5]. In this case, the objectives are the minimum of the mean square deviations.

The fit procedure starts with a random choice of the seven parameters in model equations (5), and the random choice of the initial conditions $PF(t = 10.5) = PF_0$ and $QF(t = 10.5) = QF_0$. The initial condition for ECM is assumed to be zero, $ECM(t = 10.5) = 0$. Then, for this choice of parameters, we test if the steady state (6) is stable. If the real parts of all the eigenvalues of the Jacobian matrix (7) are negative, we accept these parameters as an eventual solution of the optimization

problem. For each random choice of acceptable parameters and initial conditions, we calculate the mean square deviations from the PF and ECM data sets. After iterating this procedure $100,000$ times, for random choices of the parameter values, we calculate the solutions on the Pareto front obtained from the mean square deviation pairs. Then, one solution on the Pareto front is chosen.

The parameter values and initial conditions that fit the experimental data in Tables 1 and 2 are depicted in Table 3. In Figure 2C, we show the experimental data and the solutions obtained with model equations (5) with the parameters in Table 3. The immediate conclusion is that the negative feedback loop resulting from the catalytic model summarized in Figure 2A and described by equations (5) describes with high accuracy the mechanism of dermis maturation.

Table 3: Parameter values and initial conditions for model equations (5) that fits the experimental data in Tables 1 and 2

Parameters	Fitted values
β	0.3010
k_2	1.0102
k_{-2}	0.6084
k_3	0.0610
k_4	0.2008
k_6	0.0424
k_7	0.8380
PF_0	0.3530
QF_0	0.1166

2 Wound healing

It is well established that upon wounding dermal fibroblasts become activated and re-start proliferating[6]. As our model proposes a negative feedback mechanism describing the interaction between PF and ECM, we decided to investigate the dynamic mechanism of regeneration when the local steady state is perturbed, as in the case of a wound for example.

In our model, the system of equations (5) describes the local concentration of cells in the dermis during maturation and homeostasis assuming that the structure of the dermis is spatially homogeneous. To describe the wound healing mechanism, we assume that after wounding the regeneration process is initiated with the motility of fibroblasts at the boundary of the wound. The closer to the wound, the more the system is away from the steady state (6). The simplest mechanism to describe regeneration is to assume that at the wound region there is diffusion of PF and QF cells, dynamically regenerating the structure of the dermis. On the other hand, as ECM is a mixture of proteins, it is also plausible to assume that it has low motility, in the sense that it is deposited near quiescent fibroblasts. In this case, the wound healing mechanism is only associated with the motility of the PF and QF cells. Under these conditions, the spatial structure of the dermis is described by the partial differential system of equations

$$\begin{cases} \frac{dPF}{dt} = \beta PF + k_{-2}QF - k_4 ECM\ PF + D\frac{\partial^2 PF}{\partial x^2} \\ \frac{dQF}{dt} = k_2 PF - k_{-2}QF + k_4 ECM\ PF - k_6 QF + D\frac{\partial^2 QF}{\partial x^2} \\ \frac{dECM}{dt} = k_3 QF - k_7 ECM \end{cases} \tag{8}$$

where the constant D is a diffusion coefficient, equal for both PF and QF cells. To simplify, we have considered that dermis is developed along a one-dimensional domain, with periodic boundary conditions (circular domain). Due to the simplicity of our assumptions, we can only test qualitatively the results of the model. We will not consider the case of periodic boundaries conditions and a more detailed mathematical analysis of the model equations will be developed in a subsequent publication.

To be more specific, we consider the one-dimensional spatial domain of length $L = 1$. This spatial domain represents the dermis. We also assume that the parameter values in Table 3 still hold. The situation we want to analyse is the mechanism driving the changes in the cell density inside the wound. For that, we consider that a normal dermis is characterised by a uniform concentration of fibroblasts and extracellular matrix in steady state. To test the model, we further consider a wound in the spatial region $x \in [0.45, 0.5]$. In this case, the wounded tissue is represented by the initial conditions in (9):

$$\begin{cases} PF(x, t=0) = PF^* \text{ for } x \in [0, 0.45] \text{ and } x \in [0.5, 1], \text{ and } PF(x, t=0) = 0, \text{ otherwise} \\ QF(x, t=0) = QF^* \text{ for } x \in [0, 0.45] \text{ and } x \in [0.5, 1], \text{ and } QF(x, t=0) = 0, \text{ otherwise} \\ ECM(x, t=0) = ECM^* \text{ for } x \in [0, 0.45] \text{ and } x \in [0.5, 1], \text{ and } ECM(x, t=0) = 0, \text{ otherwise} \end{cases} \tag{9}$$

In this formulation PF, QF and ECM are densities. The initial conditions (9) are not a steady state solution of the partial differential equation (8) and therefore the local densities evolve with time.

To integrate the partial differential equation system (8), from the initial conditions (9), we used a calibrated numerical method for reaction-diffusion equations[7] and we chose a diffusion coefficient in such a way that the percentage of fibroblasts is attained by day 4.5 after wounding, in agreement with the experimental results of Figure 5A. After several numerical tests, we estimated the diffusion coefficient to be $D = 2.10^{-4} cm^2/day$. We show in Figure 5E the temporal evolution of the percentage of fibroblasts and extracellular matrix inside the wound, where we can observe that the results are qualitatively similar to the experimental data in Figure 5A. The values of fibroblasts and extracellular matrix inside the wound were calculated by:

$$\begin{cases} \overline{PF}(t) = \int_{0.45}^{0.5} PF(x,t)dx \\ \overline{QF}(t) = \int_{0.45}^{0.5} QF(x,t)dx \\ \overline{ECM}(t) = \int_{0.45}^{0.5} ECM(x,t)dx \\ \overline{PF}(t) = 100 \frac{\overline{PF}(t)}{\overline{PF}(t)+\overline{QF}(t)} \end{cases} \tag{10}$$

where $PF(x,t)$, $QF(x,t)$ and $ECM(x,t)$ are the numerical solutions of equations (10).

References

[1] Whitman, M. & Melton, D. A. Growth Factors In Early Embryogenesis. *Annual Review of Cell Biology* **5**, 93–117 (1989).

[2] Driskell, R. R. *et al.* Distinct fibroblast lineages determine dermal architecture in skin development and repair. *Nature* **504**, 277–281 (2013).

[3] Dilão, R. & Muraro, D. A software tool to model genetic regulatory networks. Applications to the modeling of threshold phenomena and of spatial patterning in Drosophila. *PLoS ONE* **5**, e10743 (2010).

[4] Dilão, R., Muraro, D., Nicolau, M. & Schoenauer, M. Validation of a Morphogenesis Model of Drosophila Early Development by a Multi-objective Evolutionary Optimization Algorithm. *EvoBIO* (2009).

[5] Muraro, D. & Dilão, R. A parallel multi-objective optimization algorithm for the calibration of mathematical models. *Swarm and Evolutionary Computation* **8**, 13–25 (2013).

[6] Rognoni, E. *et al.* Inhibition of β-catenin signalling in dermal fibroblasts enhances hair follicle regeneration during wound healing. *Development* dev.131797 (2016).

[7] Dilão, R. & Sainhas, J. Validation and Calibration of Models for Reaction–Diffusion Systems. *International Journal of Bifurcation and Chaos* **08**, 1163–1182 (2011).